



BNL-225462-2024-JAAM

GRP-COEE-31

Healable and conductive sulfur iodide for solid-state Li-S batteries

J. Zhou, E. Hu

To be published in "Nature"

March 2024

Chemistry Department
Brookhaven National Laboratory

U.S. Department of Energy

USDOE Office of Energy Efficiency and Renewable Energy (EERE), Office of Sustainable
Transportation. Vehicle Technologies Office (VTO)

Notice: This manuscript has been authored by employees of Brookhaven Science Associates, LLC under Contract No. DE-SC0012704 with the U.S. Department of Energy. The publisher by accepting the manuscript for publication acknowledges that the United States Government retains a non-exclusive, paid-up, irrevocable, world-wide license to publish or reproduce the published form of this manuscript, or allow others to do so, for United States Government purposes.

DISCLAIMER

This report was prepared as an account of work sponsored by an agency of the United States Government. Neither the United States Government nor any agency thereof, nor any of their employees, nor any of their contractors, subcontractors, or their employees, makes any warranty, express or implied, or assumes any legal liability or responsibility for the accuracy, completeness, or any third party's use or the results of such use of any information, apparatus, product, or process disclosed, or represents that its use would not infringe privately owned rights. Reference herein to any specific commercial product, process, or service by trade name, trademark, manufacturer, or otherwise, does not necessarily constitute or imply its endorsement, recommendation, or favoring by the United States Government or any agency thereof or its contractors or subcontractors. The views and opinions of authors expressed herein do not necessarily state or reflect those of the United States Government or any agency thereof.

Healable and Conductive Sulfur Iodide for Solid-State Li-S Batteries

Jianbin Zhou,^{1,11} Manas Likhit Holekevi Chandrappa,^{1,11} Sha Tan,² Shen Wang,¹ Chaoshan Wu,³ Howie Nguyen,⁴ Canhui Wang,⁵ Haodong Liu,¹ Sicen Yu,¹ Quin R. S. Miller,⁶ Gayea Hyun,¹ John Holoubek,¹ Junghwa Hong,¹ Yuxuan Xiao,⁷ Charles Soulen,¹ Zheng Fan,⁸ Eric E. Fullerton,⁷ Christopher J. Brooks,⁹ Chao Wang,⁵ Raphaële J. Clément,⁴ Yan Yao,³ Enyuan Hu,² Shyue Ping Ong,^{1,10*} Ping Liu^{1,10*}

¹Department of Nanoengineering, University of California, San Diego, La Jolla, CA, USA.

²Chemistry Division, Brookhaven National Laboratory, Upton, NY, USA.

³Materials Science and Engineering Program and Texas Center for Superconductivity at the University of Houston, University of Houston, Houston, TX, USA.

⁴Materials Department and Materials Research Laboratory, University of California, Santa Barbara, CA, USA.

⁵Department of Chemical and Biomolecular Engineering, Johns Hopkins University, Baltimore, MD, USA.

⁶Energy and Environment Directorate, Pacific Northwest National Laboratory, Richland, WA, USA.

⁷Center for Memory and Recording Research, University of California, La Jolla, San Diego, CA, USA

⁸Department of Engineering Technology, University of Houston, Houston, TX 77204, USA

⁹Honda Development and Manufacturing of America, North American Auto Development Center, 21001 OH-739, Raymond, OH 43067-9705, USA

¹⁰Sustainable Power and Energy Center, University of California, San Diego, La Jolla, CA, USA

¹¹These authors contribute equally to this work.

*Corresponding author. Email: piliu@ucsd.edu (P.L.), ongsp@ucsd.edu (S.P.O.)

Solid-state Li-S batteries (SSLSBs) are made of low cost and abundant materials free of supply chain concerns. Due to their high theoretical energy densities, they are highly desirable for electrical vehicles¹⁻³. However, the development of SSLSBs has been historically plagued by the insulating nature of sulfur^{4,5} and the poor interfacial contacts induced by its large volume change during cycling^{6,7}, impeding charge transfer among different solid components. Here, we report a S_{9.3}I molecular crystal with I₂ inserted in the crystalline S structure, which shows a semiconductor-level electrical conductivity ($\sim 5.9 \times 10^{-7}$ S cm⁻¹) at 25 °C, an 11 order of magnitude increase over S itself. Iodine introduces new states into the band gap of S and promotes the formation of reactive polysulfides during electrochemical cycling. Further, the material features a low melting point of ~65 °C, which enables repairing damaged interfaces due to cycling by periodical re-melting of the cathode material. As a result, a Li-S_{9.3}I battery demonstrates 400 stable cycles with a specific capacity retention of 87%. The design of this conductive, low-melting-point sulfur iodide material represents a substantial advancement in the chemistry of S materials, and opens the door to the practical realization of SSLSBs.

SSLSBs with inorganic solid electrolytes (SEs) do not suffer from the capacity fade associated with the “polysulfide shuttle” phenomenon in liquid electrolytes^{8,9}. They involve direct conversion between S and Li₂S during cycling^{4,10}, and rely entirely on the interfaces between the SEs, conductive carbon, and S species to transfer charge^{11,12}. This reliance paired with the insulating nature of S (electrical conductivity of $\sim 5 \times 10^{-18}$ S cm⁻¹) is untenable. Further, S expands by ~79% when converted to Li₂S, leading to failures of solid/solid interfaces (Extended data Fig.1a) ^{13,14}. In contrast, a liquid/solid interface always maintains perfect contact. In this regard, a sulfur material with intrinsic conductivity and a low melting point will allow for the initial formation and subsequent re-formation of perfect interfaces (Extended data Fig. 1b).

S_{9.3}I is readily synthesized by grinding stoichiometric amounts of S and I₂ powder in air and

heating the mixture to 80 °C in a sealed container (Extended data Fig. 1c). The melting point of S_{9.3}I is ~ 65 °C as confirmed by differential scanning calorimetry (DSC, Extended data Fig. 1d) and in-situ X-ray diffraction (XRD, Extended data Fig. 1e). Scanning electron microscopy (SEM) combined with energy-dispersive X-ray spectroscopy (EDX) mapping (Extended data Fig. 1g-i) indicates that the as-prepared S_{9.3}I solid has a homogeneous distribution of S and I. S_{9.3}I appears to be a unique composition based on DSC analysis, where residual S or I₂ is observed except for the 9.3:1 ratio. These results are also consistent with the Raman spectra (Extended data Fig. 1f).

The XRD pattern of S_{9.3}I (Fig. 1a) appears to be very similar to that of S in the wide-angle region, but has a prominent broad peak centered at ~1.5°. This peak corresponds to a d-spacing of 5.8 nm, indicative of the formation of a superstructure. More information on the XRD analysis can be found in the Extended data Fig. 1j. Atomic pair distribution function analysis (PDF, Fig. 1b) shows an absence of I₂ with long range ordering, but I-I remains after melting. In S PDF, the peaks at around 2.0 Å, 3.3 Å, and 4.5 Å correspond to unique correlations within the S₈ puckered ring. Their dominance along with the presence of the 2.7 Å peak in the S_{9.3}I PDF suggest the structure is mainly composed of S₈ rings with the insertion of I₂ molecules. The mass spectra of S_{9.3}I and S further show that I₂ molecules are inserted into the S structure (Extended data Fig. 1k). Additional PDF of sulfur iodide with different S:I ratios (Extended data Fig. 1l) are consistent with the DSC, XRD and Raman data. Moreover, solid S_{9.3}I has a density of 2.45 g cm⁻³, slightly higher than that of sulfur (2.07 g cm⁻³). The material density remains rather constant in its liquid (~2.35 g cm⁻³) and solid states, essential for using the re-melting method to repair microstructural damages.

To elucidate the structure of S_{9.3}I, density functional theory (DFT) calculations are performed by using the Strongly Constrained and Appropriately Normed (SCAN) meta-GGA functional. The SCAN functional yields better agreement with experimental cell parameters for S (Extended data Table 1) and has been extensively benchmarked on the energetics and structure relaxations of diversely

bonded materials¹⁵. The calculations were performed on candidate structures wherein S₈ rings (atomic mass = 256.48 g mol⁻¹) within orthorhombic octasulfur are substituted by linear I₂ (253.8 g mol⁻¹) or I₃ (380.7 g mol⁻¹) molecules, spanning a compositional range from S₆₀I (one I₂ substituting for a single S₈ unit in the octasulfur unit cell) to S₈I (six I₂ replacing four S₈ units). We find that the lowest energy configuration of the S_{9.6}I composition (five I₂ replacing four S₈ units) is close to the experimental S_{9.3}I composition, has a small energy above hull of 13 meV atom⁻¹ (Fig. 1c). It is well within the typical energy range of thermal contributions at room temperature (~25 meV atom⁻¹) and typical thresholds of energies above hull used to ascertain potential synthesizability of materials (~50 meV atom⁻¹)¹⁶. The relaxed S_{9.6}I configuration has a negligible 3% volume shrinkage and a higher computed density of 2.21 g cm⁻³ compared to bulk S, which is consistent with the experimental observations. The computed XRD patterns also feature a peak at low angles, indicative of a super structure (Extended data Fig. 2a). The computed PDF of S_{9.6}I structure matches well with the experimental data with major peaks present at 2, 2.7 and 3.4 Å (Extended data Fig. 2b). We also note that the SCAN lattice energy of S_{9.6}I (-361 meV molecule⁻¹) is ~40 meV molecule⁻¹ smaller than that of S (-400 meV molecule⁻¹). This suggests that I₂ incorporation disrupts the van der Waals interactions in S₈, which contributes to the lowered melting point. The structures in the S_{9.6}I-S₈I compositional space are also analyzed to understand the broader impact/trend of I₂ substitution (Extended data Fig. 2c). Unless specified, the results of S_{9.6}I composition hold for all these compositions.

Using Bader charge analysis, we quantified the charge transfer between S and I in S_{9.6}I by calculating the net difference between the charge on an I atom in S_{9.6}I and the number of valence electrons in atomic I. A small charge transfer of 0.067 electrons is found, indicating limited charge transfer. This is corroborated by the experimental S K-edge and I L₂-edge X-ray absorption spectroscopy (XAS, Fig. 1d). Changes in electronic structure of S upon formation of S_{9.3}I are further probed by electron paramagnetic resonance (EPR). In-situ EPR spectra during heating from 20 °C to 150 °C (Extended data Fig. 3a-b) reveal the radical concentration in S_{9.3}I grows with increasing

temperature, in contrast, no EPR signal is obtained from pure S. The high level of radicals in $S_{9.3}I$ (Extended data Fig. 3c) motivates us to measure its electrical conductivity, which is found to be 5.9×10^7 S cm⁻¹ at 25 °C (Fig. 1e and Extended data Fig. 3d-f), an 11 orders of magnitude increase over elemental S. This observation can be rationalized by visualizing the computed partial density of states (PDOS) of S and $S_{9.6}I$. Pure S has a Heyd-Scuseria-Ernzehof (HSE) functional band gap of 2.92 eV (Extended data Fig. 2d), slightly higher than experimental values of 2.4-2.7 eV reported previously^{17,18}. The introduction of I_2 adds states within the gap and reduces the HSE band gap to 1.65 eV (Fig. 1f). A qualitatively similar result is obtained for SCAN functional (Extended data Fig. 2e-f). There is only a small overlap between the S and I states, consistent with the fact that little charge transfer is observed between S_8 and I_2 . We find that there is a monotonic decrease in the band gap with increasing I concentration (Extended data Fig. 2d). We note that iodine itself has semiconducting properties due to electronic interactions between neighboring I_2 molecules, and we believe that such interactions also occur in sulfur iodides. This decrease in the band gap upon introducing I_2 species into the system explains the increase in conductivity from elemental S to $S_{9.6}I$. Additionally, the absence of partially filled bands and the limited charge transfer between S_8 and I_2 molecules suggest that sulfur iodide is a thermodynamically metastable material rather than a dynamically stabilized one¹⁹.

$S_{9.3}I$ is evaluated in a solid state battery with Li_3PS_4 (LPS) as the electrolyte. The cathode composite is melted at 100 °C to achieve excellent interfacial contact (Extended data Fig. 4). LPS is chosen as it is found to contribute limited capacity (Extended data Fig. 5a-d). Super P carbon (SP) is applied as an interlayer between Li and SE to stop the growth of Li dendrites (Extended data Fig. 5e-f), which is inspired by the Ag/C interlayer design reported previously²⁰. We note that there are other promising approaches to address the Li anode stability issue²¹. Further details are provided in the Methods.

The Li- $S_{9.3}I$ cell (Fig. 2a) is cycled at a current density of 0.16 A g⁻¹ and at different temperatures. Specific capacities ranging from 811.8 to 1211.3 mAh g⁻¹ are delivered from 25 to 100

°C. Increasing the operating temperature greatly enhances cell kinetics as demonstrated by smaller polarization and higher capacities. The stability of the cells operating above the melting point of S_{9.3}I is enabled by its high viscosity coupled with our cell design (see Methods). In contrast, the elemental S cathode (Fig. 2b) delivers much lower capacities, likely due to its poor electronic conductivity. The dQ/dV profiles of S cathode show one redox reaction plateau (Extended data Fig. 6a-b), while S_{9.3}I shows two, implying their distinct working mechanisms. The two plateaus for S_{9.3}I are most likely related to the polysulfide intermediates that are absent in the S cathode reactions. S_{9.3}I exhibits the most stable and highest capacity compared to materials with other S:I ratios (Extended data Fig. 6c-d). Moreover, a capacity of 489.4 mAh g⁻¹ is delivered even at a rate of 5.60 A g⁻¹, compared favorably with reported SSLSBs (Extended data Fig. 6e-g and Table 2)^{9,13,22-29}. At a loading of 4.2 mg cm⁻² of S_{9.3}I, the cathode still delivers a specific capacity of 968.5 mAh g⁻¹ after 50 cycles at 0.32 A g⁻¹ (Extended data Fig. 6h-i). The anode interface is still well maintained and Li is deposited underneath the SP interlayer (Extended data Fig. 7).

Long-term cycling performance at room temperature is critical towards the practical application of SSLSBs. When cycled at a current density of 0.16 A g⁻¹ (Fig. 2c), the capacity of the S_{9.3}I cathode increases slightly due to progressive activation during the initial 10 cycles, but decays to 794.6 mAh g⁻¹ by the 50th cycle. This fade is attributed to degradation of the cathode interfaces and can be addressed by briefly re-melting the cathode at 100 °C before cycling again at 25 °C, where the full cell capacity recovers to 828.1 mAh g⁻¹. In this regard, the Li-S_{9.3}I full cell can be periodically repaired in-situ over its lifetime. By heat treating the cell every 50 cycles, a capacity of 701 mAh g⁻¹ (87% retention) and an average coulombic efficiency of ~99.8% are maintained after 400 cycles, outperforming other reported SSLSBs (Extended data Fig. 6j and Table 2). The voltage profiles (Fig. 2d) at different cycles indicate minimal polarization increase. Moreover, S_{9.3}I cathodes at 40, 60, and 80 °C also show excellent coulombic efficiency and cycling stability (Extended data Fig. 6k-m). Electrochemical impedance spectroscopy (EIS) results confirm the enhancement in electrode kinetics

for $S_{9.3}I$ over S (Extended data Fig. 8). The remarkable electrical conductivity and melt-driven interface repair provided by the $S_{9.3}I$ cathode result in accelerated electrochemical reaction kinetics, solving many of the operational challenges of SSLSBs.

To probe the working mechanism of the $S_{9.3}I$ cathode, Fig. 3a shows the S K-edge XAS of the cathode at different states of charge. The S–S π^* feature in S_8 ³⁰ shifts to lower energy levels, corresponding to the formation of short chain LiS_x when discharged to 1.7 V (D-1.7 V), and further shifts to those attributed to Li_2S and long chain LiS_x when discharged to 1.3 V (D-1.3 V). This process is fully reversible, as S_8 features are recovered upon charge to 3.0 V (C-3.0 V). This reversibility is also corroborated with the S_{2p} XPS spectra (Fig. 3b). In the pristine state, only S_0 (elemental S, 163.9 eV) and S_p (LPS, 162.0 eV) signals can be resolved³¹. On discharge to 1.7 V, the peak intensity of S_0 decreases and the peaks assigned to S_b (bridge S in LiS_x , 163.5 eV), S_t (terminal S in LiS_x , 161.7 eV) and S_{2-} (Li_2S , 160.5 eV) increase^{32,33}. When further discharged to 1.3 V, S_0 peak disappears, S_b and S_t peaks decrease, and the S_{2-} peak increases. XPS confirms the good reversibility shown in the XAS data, again returning to the pristine state after charging to 3.0 V (Extended data Fig. 9a). The excellent reversibility of $S_{9.3}I$ cathode is also demonstrated by ex-situ Raman (Extended data Fig. 9b) and ex-situ EPR (Extended data Fig. 9c-f).

To probe the mechanism further, a chemically lithiated $S_{9.3}I$ prepared at an equivalent discharge capacity of ~ 800 mAh g⁻¹ (see Methods) is shown to contain large amounts of long chain LiS_x along with Li_2S as indicated by XAS (Fig. 3a) and XPS (Extended data Fig. 9g) results. In contrast, the elemental S cathode discharged to 1.3 V shows negligible amounts of LiS_x and a small amount of Li_2S . The existence of LiS_x in $S_{9.3}I$ cathodes discharged to 1.3 V and the chemically lithiated $S_{9.3}I$ are further confirmed by ultraviolet-visible (UV-Vis) spectroscopy analysis of their tetrahydrofuran (THF) solution (Extended data Fig. 9h-i). Overall, the formation of LiS_x during cycling is an essential feature of the working mechanism of $S_{9.3}I$ cathode. Additional XRD analysis confirms the presence of Li_2S in chemically lithiated $S_{9.3}I$ (Extended data Fig. 10a). Cryo-transmission electron microscopy (cryo-

TEM) EDX and Li electron energy loss spectroscopy (EELS) indicate a homogeneous distribution of S, I and Li species over the bulk area of the sample (Fig. 3c, Extended data Fig. 10b-c and Methods), implying no phase segregation. The S:I atomic ratio in lithiated $S_{9.3}I$ determined by EDX is 9.6:1, very close to the theoretical ratio.

The evolution of the cathode/electrolyte interface during cycling is investigated by cross-sectional SEM. In the as-prepared cell (Fig. 4a), the $S_{9.3}I$ cathode is ~ 19 μm -thick and displays intimate interfacial contact with the LPS layer. After 50 cycles at 25 °C, interfacial voids are observed (Fig. 4b), presumably due to the volume change of the cathode during cycling. The thickness of the cathode layer also increases to ~ 22 μm , pointing to additional porosity buildup inside the cathode composite. The electrode undergoes melt-driven in-situ interfacial repair after being heated to 100 °C followed by cooling back to 25 °C (Fig. 4c). The S: I ratio inside the cathode after repeated heating-cooling processes shows negligible change (Extended data Fig. 10d-e). Interfacial repair by heating also manifests itself in EIS (Extended data Fig. 10f-g) and Distribution of Relaxation Times (DRT) analysis (Fig. 4d). Relaxation times in the range of 0.1-1 s are associated with the impedance of ion transport across the cathode interface^{34, 35}. The interfacial impedance continuously increases from the 1st cycle to the 50th cycle, but is reduced by re-heating to the value after the 1st cycle. A similar restoration is observed at the 100th cycle as well. Re-heating is thus highly effective in healing the cathode interface as demonstrated in the cycling stability shown in Fig. 2c. Melt-driven in-situ repair of the interface is enabled by the low melting point of $S_{9.3}I$, which is supported by DSC data (Fig. 4e).

Overall, the design of this conducting sulfur iodide molecular crystal material with low melting points expands the scope of solid state chemistry of sulfur. Iodine contributes new states inside the band gap of sulfur to introduce electronic conductivity and promotes the formation of LiS_x species, which are essential in increasing the reactivity of sulfur. The discovery of the sulfur iodide material might inspire search for other sulfur materials that have even lower melting points and higher conductivities.

References

1. Bruce, P. G., Freunberger, S. A., Hardwick, L. J. & Tarascon, J. M. Li-O₂ and Li-S batteries with high energy storage. *Nat. Mater.* **11**, 19-29 (2011).
2. Randau, S. et al. Benchmarking the performance of all-solid-state lithium batteries. *Nat. Energy* **5**, 259-270 (2020).
3. Yang, Z., Huang, H. & Lin, F. Sustainable electric vehicle batteries for a sustainable world: perspectives on battery cathodes, environment, supply Chain, manufacturing, life cycle, and policy. *Adv. Energy Mater.* **12**, 2200383 (2022).
4. Yue, J., Yan, M., Yin, Y. X. & Guo, Y. G. Progress of the interface design in all-solid-state Li-S batteries. *Adv. Funct. Mater.* **28**, 1707533 (2018).
5. Guo, W. et al. Artificial dual solid-electrolyte interfaces based on in situ organothiol transformation in lithium sulfur battery. *Nat. Commun.* **12**, 3031 (2021).
6. Fu, K. et al. Three-dimensional bilayer garnet solid electrolyte based high energy density lithium metal–sulfur batteries. *Energy Environ. Sci.* **10**, 1568-1575 (2017).
7. Lin, Z., Liu, Z. C., Dudney, N. J. & Liang, C. D. Lithium superionic sulfide cathode for all-solid lithium-sulfur batteries. *ACS Nano* **7**, 2829–2833 (2013).
8. Ji, X., Lee, K. T. & Nazar, L. F. A highly ordered nanostructured carbon-sulphur cathode for lithium-sulphur batteries. *Nat. Mater.* **8**, 500-506 (2009).
9. Pan, H. et al. Carbon-free and binder-free Li-Al alloy anode enabling an all-solid-state Li-S battery with high energy and stability. *Sci. Adv.* **8**, eabn4372 (2022).
10. Yang, X., Luo, J. & Sun, X. Towards high-performance solid-state Li-S batteries: from fundamental understanding to engineering design. *Chem. Soc. Rev.* **49**, 2140-2195 (2020).
11. Wu, J., Liu, S., Han, F., Yao, X. & Wang, C. Lithium/sulfide all-solid-state batteries using sulfide electrolytes. *Adv. Mater.* **33**, 2000751 (2021).

12. Nagao, M., Hayashi & Tatsumisago, A. M. High-capacity Li_2S –nanocarbon composite electrode for all-solid-state rechargeable lithium batteries. *J. Mater. Chem.* **22**, 10015–10020 (2012).
13. Chen, Z. et al. Bulk/interfacial synergistic approaches enable the stable anode for high energy density all solid-state lithium–sulfur batteries. *ACS Energy Lett.* **7**, 2761–2770 (2022).
14. Yao, X. et al. High performance all-solid-state lithium–sulfur batteries enabled by amorphous sulfur-coated reduced graphene oxide cathodes. *Adv. Energy Mater.* **7**, 1602923 (2017).
15. Saßnick, H. D. & Cocchi, C. Electronic structure of cesium-based photocathode materials from density functional theory: performance of PBE, SCAN, and HSE06 functionals. *Electron. Struct.* **3** 027001 (2021).
16. Hautier, G. et al. Phosphates as lithium-ion battery cathodes: an evaluation based on high-throughput ab initio calculations. *Chem. Mater.* **23**, 15, 3495–3508 (2011).
17. Liu, G., Niu, P., Yin, L. & Cheng, H. M. alpha-Sulfur crystals as a visible-light-active photocatalyst. *J. Am. Chem. Soc.* **134**, 9070–9073 (2012).
18. Abass, A. K. & Ahmad, N. H. Indirect band gap investigation of orthorhombic single crystals of sulfur. *J. Phys. Chem. Solids* **47**, 143–145. (1986).
19. Chen X. et al. Dynamically preferred state with strong electronic fluctuations from electrochemical synthesis of sodium manganite. *Matter* **5**, 735–750 (2022).
20. Lee, Y. G. et al. High-energy long-cycling all-solid-state lithium metal batteries enabled by silver–carbon composite anodes. *Nat. Energy* **5**, 299–308 (2020).
21. Ye, L. & Li, X. A dynamic stability design strategy for lithium metal solid state batteries. *Nature*, **593**, 218–222 (2021).
22. Li, C. et al. A quasi-intercalation reaction for fast sulfur redox kinetics in solid-state lithium–sulfur batteries. *Energy Environ. Sci.* **15**, 4289–4300 (2022).
23. Zhang, H. et al. Designer anion enabling solid-state lithium-sulfur batteries. *Joule* **3**, 1689–1702

(2019).

24. Zhang, Y. et al. Se as eutectic accelerator in sulfurized polyacrylonitrile for high performance all-solid-state lithium-sulfur battery. *Energy Storage Mater.* **21**, 287-296 (2019).
25. Li, X. et al. High-performance Li- SeS_x all-solid-state lithium batteries. *Adv. Mater.* **31**, 1808100 (2019).
26. Li, M. et al. Solid-state lithium–sulfur battery enabled by thio-LiSICON/polymer composite electrolyte and sulfurized polyacrylonitrile cathode. *Adv. Funct. Mater.* **30**, 1910123 (2020).
27. Wang, D. et al. Realizing high-capacity all-solid-state lithium-sulfur batteries using a low-density inorganic solid-state electrolyte. *Nat. Commun.* **14**, 1895 (2023).
28. Yao, X. et al. High performance all-solid-state lithium–sulfur batteries enabled by amorphous sulfur-coated reduced graphene oxide cathodes. *Adv. Energy Mater.* **7**, 1602923 (2017).
29. Liu, Y., Meng, X., Wang, Z. & Qiu, J. A Li_2S -based all-solid-state battery with high energy and superior safety. *Sci. Adv.* **8**, eabl8390 (2022).
30. Patel, M. U. et al. X-ray absorption near-edge structure and nuclear magnetic resonance study of the lithium-sulfur battery and its components. *Chemphyschem* **15**, 894-904 (2014).
31. Liang, X. et al. A highly efficient polysulfide mediator for lithium-sulfur batteries. *Nat. Commun.* **6**, 5682 (2015).
32. Nandasiri, M. I. et al. In-situ chemical imaging of solid-electrolyte interphase layer evolution in Li–S batteries. *Chem. Mater.* **29**, 4728-4737 (2017).
33. Yang, C. et al. Unique aqueous Li-ion/sulfur chemistry with high energy density and reversibility. *Proc. Natl. Acad. Sci. U. S. A.* **114**, 6197-6202 (2017).
34. Li, X. et al. Highly Stable Halide-electrolyte-based all-solid-state Li-Se batteries. *Adv. Mater.* **34**, 2200856 (2022).
35. Lu, Y., Zhao, C. Z., Huang, J. Q. & Zhang, Q. The timescale identification decoupling complicated kinetic processes in lithium batteries. *Joule* **6**, 1172-1198 (2022).

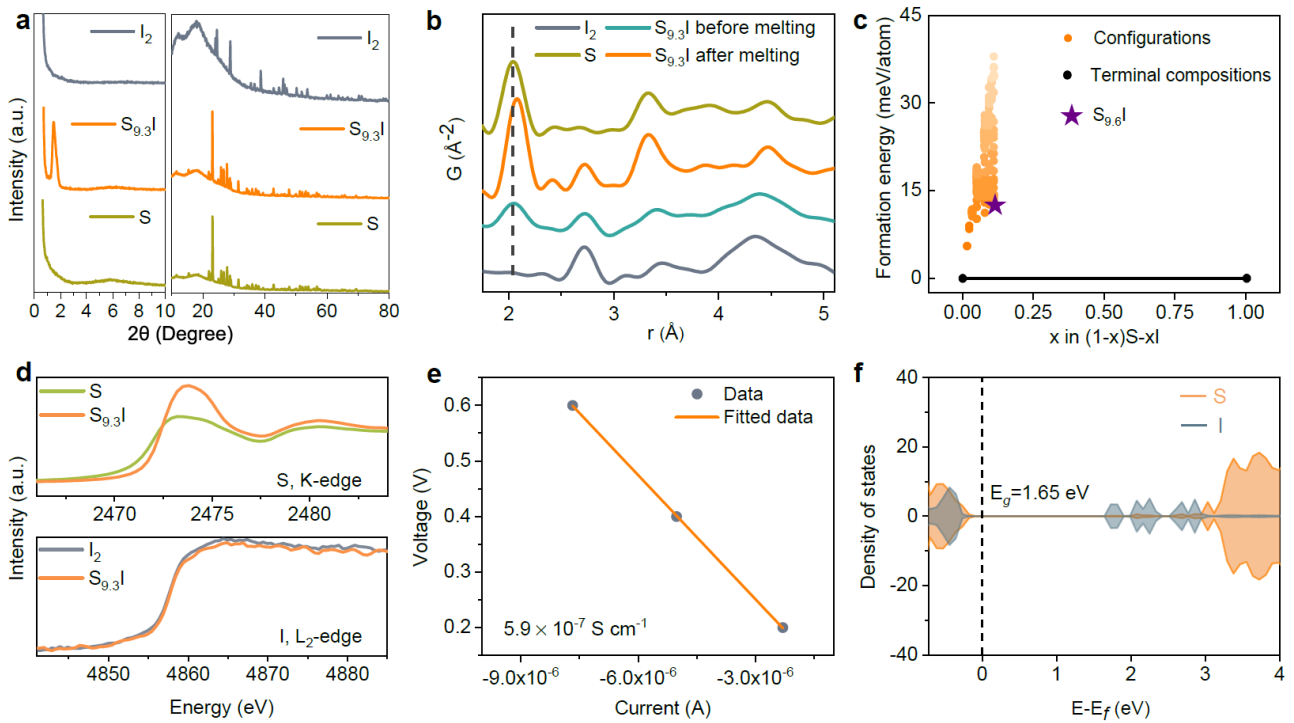


Fig. 1| Structure and property characterizations of $\text{S}_{9.3}\text{I}$. (a) XRD ($\text{K}\alpha \lambda = 1.5418 \text{ \AA}$) of S , $\text{S}_{9.3}\text{I}$ and I_2 . (b) PDF analysis of S , I_2 , and $\text{S}_{9.3}\text{I}$ before and after initial melting. (c) The pseudo-binary S-I phase diagram. (d) S K-edge and I L_2 -edge XAS data of elemental S , I_2 and $\text{S}_{9.3}\text{I}$. (e) Electrical conductivity of $\text{S}_{9.3}\text{I}$ at 25 °C, measured by the equilibrium current vs. applied voltages. (f) Elemental projected density of states for $\text{S}_{9.6}\text{I}$ from HSE calculations.

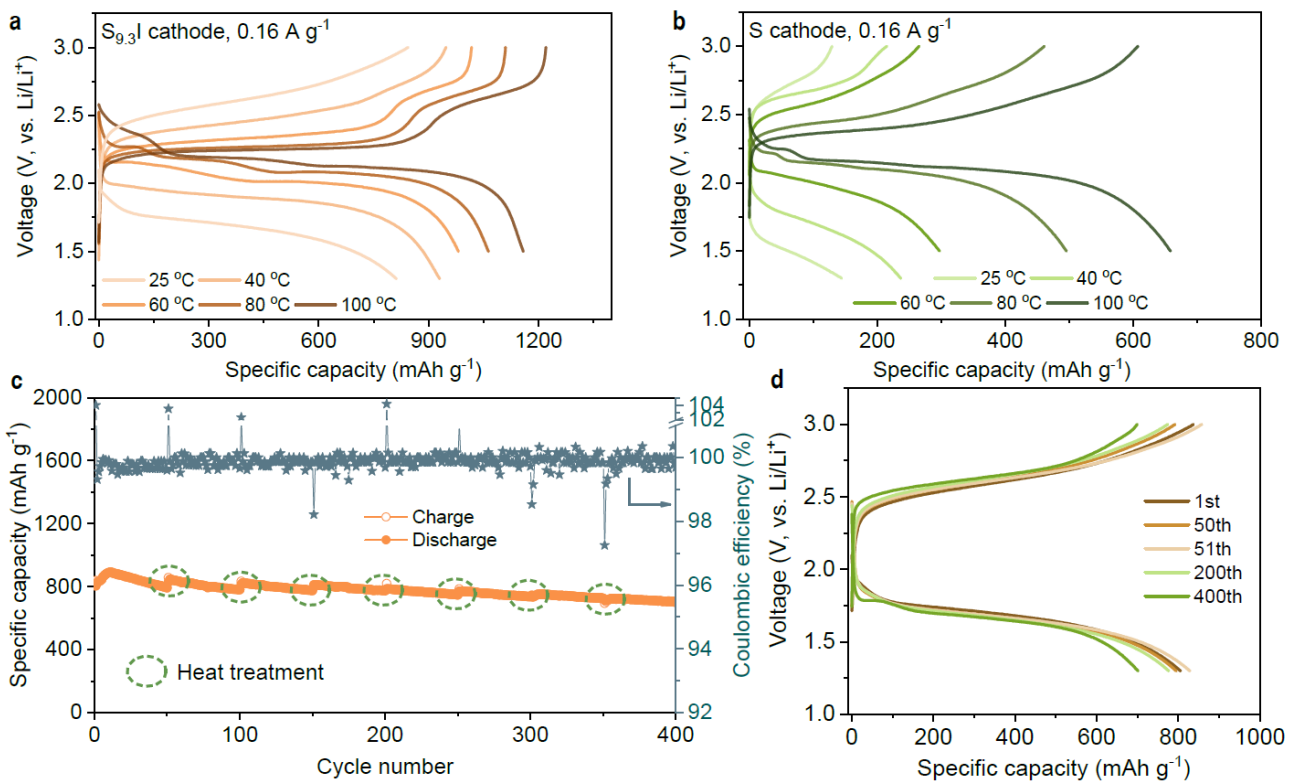


Fig. 2| The electrochemical performance of $S_{9.3}I$ and elemental S cathodes in Li-S solid state cells.

Discharge/charge profiles of (a) $S_{9.3}I$ cathode and (b) elemental S cathode at 0.16 A g^{-1} from $25 \text{ }^\circ\text{C}$ to $100 \text{ }^\circ\text{C}$. (c) Long-term cycling performance of $S_{9.3}I$ cathode at 0.16 A g^{-1} and at $25 \text{ }^\circ\text{C}$. (d) Corresponding voltage profiles at different cycles from (c).

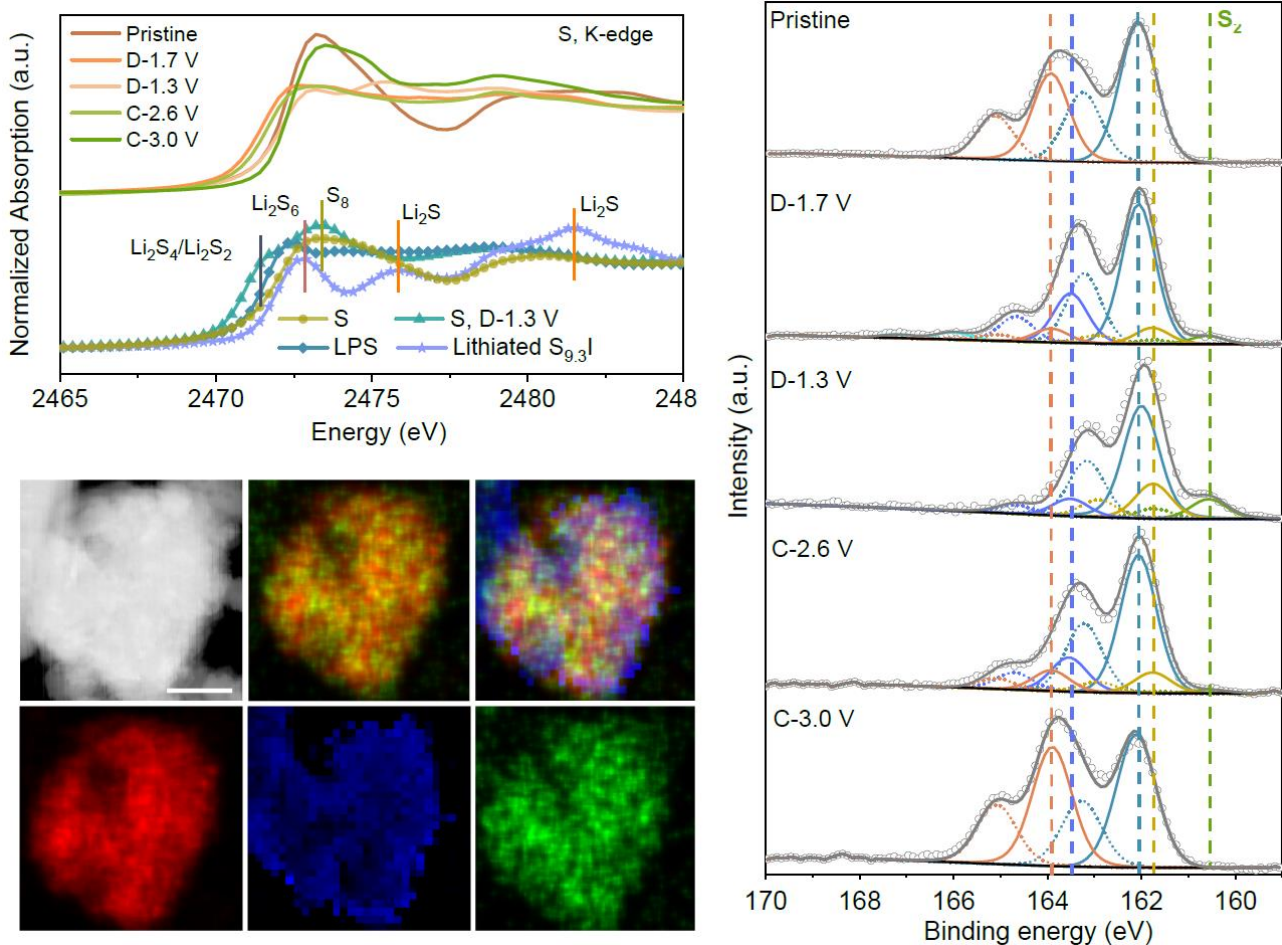


Fig. 3| The working mechanism of S_{9.3}I cathode in Li-S_{9.3}I cell at 25 °C. (a) S K-edge XAS spectra of S_{9.3}I cathode during the initial cycle. (b) S_{2p} high resolution XPS of S_{9.3}I cathode during the initial cycle. (c) Cryo-TEM HAADF, EDX and EELS mapping images of chemically lithiated S_{9.3}I. S and I maps are acquired by using EDX, Li map is acquired by using EELS.

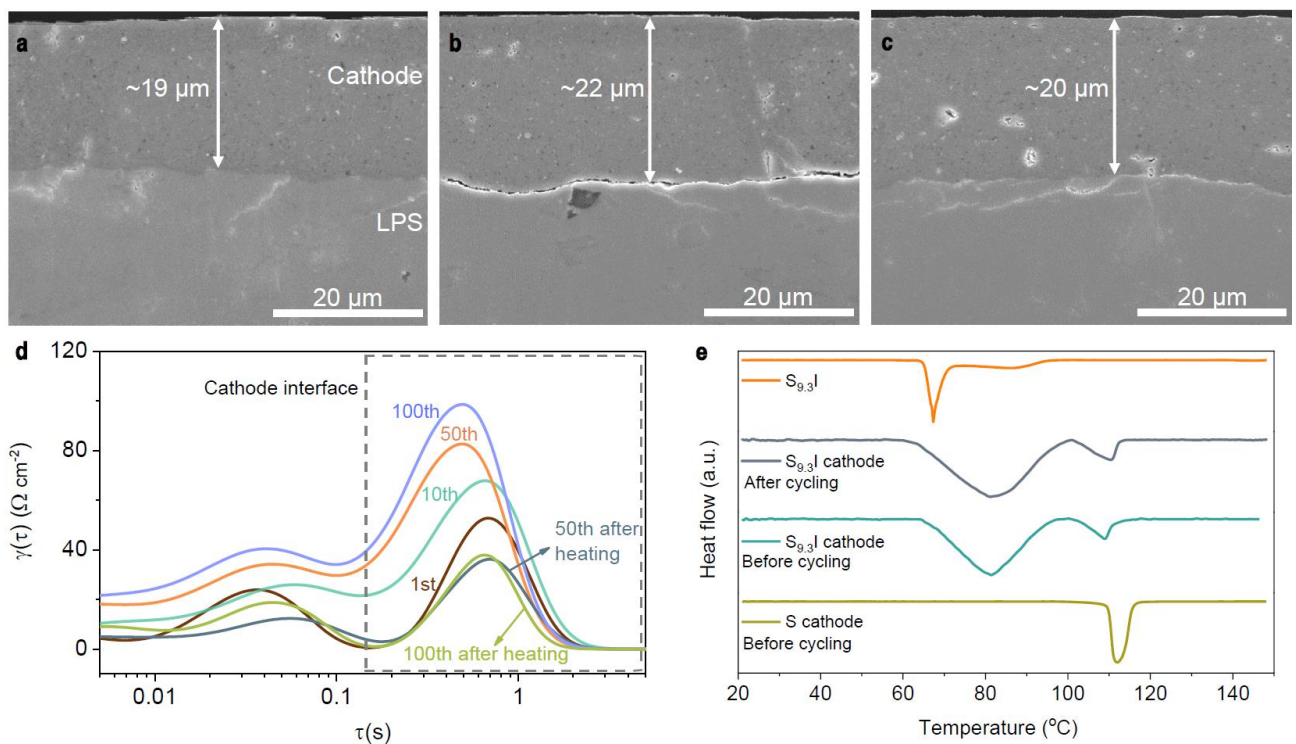


Fig. 4| Repair of the S_{9.3}I cathode/LPS SE interface in Li-S_{9.3}I cells by remelting. Cross-sectional SEM images of S_{9.3}I cathode/LPS interface at 25 °C: (a) before cycling, (b) after 50 cycles, (c) after reheating at 100 °C after 50 cycles. (d) DRT analysis of EIS data of the Li-S_{9.3}I full cell after different cycles at 25 °C. (e) DSC curves of S and S_{9.3}I cathodes before and after the initial cycle along with that of pristine S_{9.3}I.

Methods

Materials

Sulfur powder (Sigma-Aldrich, > 99.98%), iodine powder (Sigma-Aldrich, > 99.99%), vapor grown carbon fiber (VGCF, Sigma-Aldrich, > 99.99%, length: 2~10 μm , diameter: ~200 nm), Li_3PS_4 (LPS, NEI company, ion conductivity (25 °C): $\sim 1 \times 10^{-4}$ S cm^{-1} , size: 3~5 μm), $\text{Li}_6\text{PS}_5\text{Cl}$ (LPSCl, NEI company, ion conductivity (25 °C): 9.3×10^{-4} S cm^{-1} , size: 3~5 μm), Super P (SP, MTI corporation, ~40 nm), Li foils (China Energy Lithium Co., Ltd. >99.95%, ~250 μm and ~50 μm), Li powder (China Energy Lithium Co. Ltd., >97%, 25-60 μm), Tetrahydrofuran (THF, anhydrous, Sigma-Aldrich, >99.99%), Li_2S powder (Sigma-Aldrich, >99.98%).

Preparation of sulfur iodide materials

Sulfur iodide materials with different sulfur to iodine ratios are prepared by a two-step procedure. Typically, 1.0 g of S/I mixtures with different ratios are firstly prepared by grounding stoichiometric amounts of sulfur powder and iodine powder using a mortar and pestle in the air for 10 min. The sulfur iodide materials are then obtained by melting the pre-prepared S/I mixtures in a small vial (20 ml) at 80 °C for 3 h with a heating rate of 1 °C min^{-1} followed by a natural cooling procedure. The density of liquid $\text{S}_{9.3}\text{I}$ at 80 and 100 °C are measured to be ~2.35 and ~2.32 g cm^{-3} , respectively. The bulk modulus of $\text{S}_{9.3}\text{I}$ measured by compression test is 0.29 GPa at 25 °C, which is much smaller than 7.7 GPa of α - S ³⁶. The viscosity of liquid $\text{S}_{9.3}\text{I}$ increases from ~81 to ~196 mPa·s when the temperature increases from 80 to 100 °C. The behavior is associated with the increase of mass fraction of polymeric S chains that can cause more entanglement³⁷.

Preparation of $\text{S}_{9.3}\text{I}$ -LPS-VGCF cathode composite

The as-synthesized sulfur iodide pellets are crushed into powders by using mortar and pestle. A mixture composed of $\text{S}_{9.3}\text{I}$ powder, LPS and VGCF with a weight ratio of 4:4:2 is loaded into a 100 ml ball-

milling jar inside the glovebox (O_2 and moisture below 0.5 ppm) and milled at 500 rpm for 10 h. The weight ratio of ball-milling beads to the cathode composite is ~40:1. The S-LPS-VGCF cathode composite is prepared with the same procedure as the $S_{9.3}I$ -LPS-VGCF cathode.

Cells fabrication

Li/SP/LPSCl/SP/Li symmetric cells

200 mg of LPSCl powder is loaded into a PEEK die with a diameter of 13 mm and two titanium block on both sides. A pressure of ~30 MPa is applied to press the loose LPSCl powder in the die. After that, 4~5 mg cm^{-2} of SP powder is loaded on both sides of the LPSCl pellet and a high pressure of 360 MPa is applied for densification. Finally, two pieces of Li foils (~250 μm) are assembled into the symmetric cells with a pressure of ~30 MPa.

Li/SP/LPSCl/LPS/Cathode full cells

180 mg of LPS powder is loaded into a peek die with two titanium electrodes and pressed with a pressure of 30 MPa. Subsequently, 60 mg of LPSCl powder is pressed on one side of the pre-pressed LPS pellet at 30 MPa. 4 - 5 mg cm^{-2} of SP powder and ~3 mg cm^{-2} of cathode powder are then pressed on the LPSCl and LPS sides, respectively, at 30 MPa. A high pressure of 360 MPa is then used to press the SP/LPSCl/LPS/cathode composite together for 5-10 min. A piece of Li foil (~50 μm) is then attached to the SP surface to complete the assembly of the solid state full cells. A pressure of 30 MPa is maintained during cycling tests and periodical interface repair by heating. The full cells with high mass loading cathodes are assembled using the same procedure except with a mass loading of 10.5 mg cm^{-2} of the cathode composite. It should be noted that the viscosity of liquid $S_{9.3}I$ at 80 and 100 °C are ~81 and ~196 mPa·s respectively, which greatly limits its flowability in a composite cathode. To further prevent any leakage at elevated temperatures during cycling, we designed a Swagelok cell where the size difference between the Titanium piston and the PEEK die cylinder is ≤ 0.1 mm. To

prevent the liquid cathode from flowing into the LPS SSE layer, we placed the cathode at the bottom and the anode on top for battery tests when running above the melting point of the cathode. Moreover, LPS becomes much denser than LPSCl after heating at 100 °C. As a result, the Li-S_{9.3}I full cells are heat treated at this temperature before further testing. A dense LPS layer can help prevent any diffusion of the liquefied S_{9.3}I cathode, although its high viscosity makes such diffusion unlikely.

Electrochemical characterization

Before the electrochemical performance tests, all of the symmetric cells and full cells are heated at 100 °C for 3 h with a heating rate of 1 °C min⁻¹ followed by natural cooling procedures in the oven. After that, cells undergo galvanostatic cycling at different temperatures on a LAND battery test system (Wuhan, China) after resting for 3 h. To measure the long-term cycling stability of the SP interlayer for protecting lithium metal anode, a Li/Li symmetric cell is cycled at constant current density of 0.3 mA cm⁻² and a capacity of 0.3 mAh cm⁻². The EIS tests are performed on a BioLogic VMP300t electrochemical workstation within a frequency range from 7 MHz to 0.01 Hz, and the corresponding DRT analysis is performed using techniques as previously reported³⁸.

X-ray diffraction (XRD)

Small angle and wide angle x-ray diffraction (SAXRD and WAXRD) of different sulfur iodide materials are performed on a Rigaku Smartlab diffractometer with a Cu anode (K α λ = 1.5418 Å). The primary beam power is set to be 1.76 kW. The sample stage is aligned normal to the sample surface. In-situ XRD analysis (30–150 °C) of S_{9.3}I powder during heating is performed on a Bruker D8 Discover diffractometer, which is equipped with a rotating Cu anode (K α λ = 1.5418 Å) and a Vantec 500 area detector. The XRD patterns are collected every 5 °C. A borosilicate capillary (0.8 mm diameter, ~0.01 mm thin-wall, Charles Supper Co.) is used to load samples in an Ar-filled glovebox and sealed with epoxy before being taken out for tests. The sample capillary with the Ti sample holder

slit and an internal cartridge heater is placed on a custom-built programmable XYZ stage. For XRD measurements, 50 kV and 24 mA are applied. The XRD data are firstly processed with the Bruker-AXS GADDS software and further analyzed by MDI JADE XRD software.

Electrical conductivity tests

To measure the electrical conductivity of sulfur iodide materials with different ratios, 180 mg sample is pressed in a peek die (D: 13 mm) with two titanium electrodes at 360 MPa. A constant voltage of 0.2 V, 0.4 V and 0.6 V is applied for 1 hour respectively to measure the stabilized current on a BioLogic VMP300t electrochemical workstation. The thickness of the sample is confirmed by SEM. Based on the voltage, current and the thickness of samples, the electrical conductivity can be calculated.

Scanning electron microscopy (SEM)

Scanning electron microscopy (SEM, FEI Quanta 250 SEM) with an energy dispersive X-ray spectrometer (EDX) is used to determine the morphology and chemical composition of the S_{9.3}I sample under 30 kV and 0.1 nA. The cross-sectional images of S_{9.3}I/LPS and S/LPS mixture are collected by using cryo-focused ion beam-scanning electron microscopy (Cryo-FIB-SEM, FEI Scios, Scios DualBeam) operated at 5 kV and 0.1 nA. The cross-sections are first cut with an ion beam of 30 nA, followed by a surface cleaning process at 0.1 nA. For the cross-sectional SEM analysis of cathode and anode interfaces in the full cells, the samples are prepared by an Argon-ion beam cross-section polisher (IB-19520CCP) developed by JEOL. An accelerating voltage of 4 kV and a milling rate of ~25 $\mu\text{m h}^{-1}$ are used to minimize artifacts. During milling, the sample stage is placed perpendicular to the ion beam and swung automatically within $\pm 30^\circ$ to broaden the polished area and avoid beam strains. An air-free vessel is used to transfer samples between the glovebox and characterization tools. The cross-sectional SEM images of cathode and anode interfaces are conducted in Axia ChemiSEM.

Cryo-Transmission electron microscopy (TEM)

To prepare samples for the tests, a sample suspension in hexane is drop cast on a gold TEM grid in a glovebox to prevent air and water exposure. The TEM grid is then loaded on a Gatan cryo-holder in a liquid N₂ environment. The holder tip shutter is closed after loading the TEM grid on the holder and during the transfer to the microscope. The sample is kept at liquid N₂ temperature in the TEM (FEI Talos F200x microscope) to reduce radiation damage, and characterized using scanning electron microscopy transmission (STEM), energy dispersive X-ray spectrometer (EDX, FEI Super-X EDX system), and electron energy loss spectroscopy (EELS, Gatan Enfinium). The presence of Li in the sample is confirmed by EELS, which shows a peak at ~60 eV, an indication of energy loss at the Li-K edge. The presence of S and I elements in the sample are confirmed by EDX. The composite map of S, I is acquired by using EDX spectra, and the map of Li is done by EELS spectra. It should be noted that the chemically lithiated S_{9.3}I sample is still very sensitive to the electron beam even in the cryo-TEM. To reduce the beam damage, a low electron dose was applied for EDX and EELS during tests. In addition, suitable particle size should be selected to balance the needs of reducing the radiation damage and of a thinner sample for EELS signal acquisition.

X-band electron paramagnetic resonance (EPR)

X-band EPR measurements are conducted on a Bruker EMXplus EPR spectrometer. All samples are packed into Q-band tubes inside an Ar-filled glovebox and sealed with epoxy. The Q-band tubes are inserted into 4 mm quartz EPR tubes to hold the samples in place inside the resonators cavity. Variable temperature measurements are performed using an X-band Dual Mode EPR resonator (Bruker ER 4119DM). The sample is allowed to equilibrate at the desired temperatures for 10 minutes before each measurement. Measurements performed on ex-situ S_{9.3}I cathode samples at room temperature use a high sensitivity EPR resonator (Bruker ER 4119HS-LC). All measurements are carried out with 2 mW of power, a 100 kHz modulation frequency, and a modulation amplitude of 4 Gauss. Spectral fits are

conducted with EasySpin³⁹.

X-ray photoelectron spectroscopy (XPS)

The cathode layers are separated from the SSE layer by cracking the pellet cells and the conductive tapes is used to fix cathode samples on the XPS sample holders. The XPS tests are conducted on Kratos Ultra DLD to study the chemical composition and valence states of the elements in the samples with a spot size ranging 300 μm to 700 μm . All of the samples are transported into XPS equipment through a connected Ar-filled glovebox to avoid any air exposure. XPS spectra are acquired with a 0.1 eV resolution for C1s, S2p and I3d regions. The analysis of XPS spectra is performed using the CasaXPS software.

X-ray absorption spectroscopy (XAS)

The sulfur K-edge spectra are collected in fluorescence mode at 8-BM beamline of National Synchrotron Light Source II (NSLS II) at Brookhaven National Laboratory (BNL). Each spectrum takes 15 seconds, and 50 spectra are merged to get the final data for improving the signal-to-noise ratio. All the XAS results are analyzed using the Athena software package⁴⁰.

Pair distribution function (PDF)

For PDF measurement, the sample powders are packed inside polyimide capillary (Cole-Parmer) tubes sealed by epoxy glue at the end. The PDF data are collected at 28-ID-2 beamline of the NSLS II at BNL using a photon wavelength of 0.18475 \AA . The obtained data are integrated using the Fit2D software⁴¹. The PDF and G(r) values are extracted using the PDFgetX3 software⁴². For the in-situ heating PDF experiment, the sample is heated from room temperature (293 K) to 403 K, and cooled back to 293 K with a step size of 5 K.

Ultraviolet-Visible (UV-Vis) spectroscopy

Typically, 20 mg of powder samples is added into 4 ml of THF and then the THF solutions are obtained by centrifugation in several minutes. To prepare the standard Li_2S_4 and Li_2S_6 THF solutions, stoichiometric amounts of Li_2S and S powder are added into 10 ml of THF with a targeted concentration of 0.2 mmol L^{-1} . Afterwards, the solution and powder mixture are vigorously stirred over 5 days until fully dissolved. The measurements of samples are performed on a Hitachi UH4150 UV-Vis Spectrophotometer.

Differential scanning calorimetry (DSC)

10 mg of a powder sample is sealed in a $40 \mu\text{L}$ Al pan with a lid inside an Ar-filled glovebox. The samples are measured on a TA Instruments Discovery Series DSC 2500 within the temperature window of $20\text{--}150^\circ\text{C}$ at a heating rate of 5°C min^{-1} .

Raman spectroscopy

Raman measurements are performed on a Perkin Elmer Raman station 400F with a laser wavelength of 785 nm. The air sensitive samples are sealed between two quartz wafers with Kapton film covering the edges.

Mass spectrometry

Laser desorption ionization time of flight mass spectrometry (LDI-TOFMS) analysis is performed at the Molecular MS Facility at UC San Diego, by using a Bruker Autoflex Max matrix-assisted laser desorption ionization (MALDI) TOFMS instrument. The LDI-TOFMS measurement is operated under negative ion mode. Laser energy is optimized and set at 10% for “soft” ionization and minimal fragmentation. LDI-TOFMS data are acquired by using Bruker flexControl software (version 3.4) and analyzed by using Bruker flexAnalysis software (version 3.4).

Computational details

DFT parameters

The DFT calculations are carried out using the projector augmented wave (PAW) approach⁴³ as implemented in the Vienna *Ab initio* Simulation Package (VASP)⁴⁴. Structure relaxation were performed with Strongly Constrained and Appropriately Normed (SCAN) meta-GGA functional. The calculations of the electronic structure (DOS) were performed using the HSE functional⁴⁵ as well as the SCAN functional. All the calculations are spin polarized with an energy cutoff of 520 eV. The energy and force convergence criteria are set to 10^{-4} eV and 0.05 eV/Å respectively. For S unit cell and its derived structures, a Γ -centered k -points mesh of $2 \times 1 \times 1$ is used. For DOS calculations a finer k -points mesh of $2 \times 2 \times 2$ is used. The DFT-optimized minimum energy structures are used to perform Bader charge analysis⁴⁶. All the input generation and output analysis are performed using Python Materials Genomics (pymatgen)⁴⁷.

S_xI candidate structure generation

S_xI candidates at different S: I ratios are obtained by replacing S₈ rings with I₂ or I₃ molecules in octasulfur S unit cell (16 S₈ rings). The I₂ or I₃ molecules are placed at the site of S₈ rings in two possible orientations: parallel to the a-b plane along the S₈ molecular plane or perpendicular to the S₈ molecular plane. Structure enumeration is performed to obtain several distinct site orderings per composition. In addition, the effect of orientational disorder is considered by placing I₂ or I₃ molecules at different combinations of orientations. The dimension of the supercell size is 10.587 Å × 12.952 Å × 24.567 Å, which is the same as the unit cell parameter.

Data availability

The data that support the findings of this study are available from the corresponding author upon

request.

Additional references

36. Guo, Q., Lau, K. C. & Pandey, R. Thermodynamic and mechanical stability of crystalline phases of Li₂S₂. *J. Phys. Chem. C* **123**, 8, 4674-4681 (2019).
37. Sofekun, G. O. et al. The rheology of liquid elemental sulfur across the k-transition. *J. Rheol.* **62**, 469-476 (2018).
38. Wan, T., Saccoccio, H. M., Chen, C. & Ciucci, F. Influence of the discretization methods on the distribution of relaxation times deconvolution: implementing radial basis functions with DRT tools. *Electrochim. Acta* **184**, 483-499 (2015).
39. Stoll, S. & A. Schweiger. EasySpin, a comprehensive software package for spectral simulation and analysis in EPR. *J. Magn. Reson.* **178**, 42-55 (2006).
40. Ravel, B. & Newville, M. Athena, Artemis, Hephaestus: data analysis for X-ray absorption spectroscopy using IFEFFIT. *J. Synchrotron Radiat.* **12**, 537-541 (2005).
41. Hammersley, A. P., Svensson, S. O., Hanfland, M., Fitch, A. N. & Hausermann, D. Two-dimensional detector software: From real detector to idealised image or two-theta scan. *High Press. Res.* **14**, 235-248 (1996).
42. Qiu, X., Thompson, J. W., Billinge, S. J. L. PDFgetX2: a GUI-driven program to obtain the pair distribution function from X-ray powder diffraction data. *J. Appl. Crystallogr.* **37**, 678-678 (2004).
43. Blochl, P. E. Projector augmented-wave method. *Phys. Rev. B: Condens. Matter* **50**, 17953-17979 (1994).
44. Kresse, J. F. G. Efficient iterative schemes for ab initio total-energy calculations using a plane-wave basis set. *Phys. Rev. B* **54**, 1169-1186 (1996).
45. Heyd, J., Scuseria, G. E. & Ernzerhof, M. Hybrid functionals based on a screened Coulomb

potential. *J. Chem. Phys.* **118**, 8207-8215 (2003).

46. Tang, W., Sanville, E. & Henkelman, G. A grid-based Bader analysis algorithm without lattice bias. *J. Phys.: Condens. Matter* **21**, 084204 (2009).

47. S. P. Ong et al. Python materials genomics (pymatgen): A robust, open-source python library for materials analysis. *Comput. Mater. Sci.* **68**, 314-319 (2013).

Acknowledgments

This work was supported by the Advanced Research Projects Agency-Energy, U.S. Department of Energy (DOE), under Contract No. DE-AR0000781. M.L.H.C and S.P.O. acknowledge the support from the Materials Project, funded by the U.S. DOE, Office of Science, Office of Basic Energy Sciences, Materials Sciences and Engineering Division, under Contract DEAC02-05-CH11231 (Materials Project Program KC23MP). Computing resources were provided by National Energy Research Scientific Computing Center (NERSC) and the Advanced Cyberinfrastructure Coordination Ecosystem: Services & Support (ACCESS) under grant DMR150014 S.T. and E.H. are supported by the Assistant Secretary for Energy Efficiency and Renewable Energy (EERE), Vehicle Technology Office of the US DOE through the Advanced Battery Materials Research (BMR) Program under contract no. DE-SC0012704. This research used 28-ID-2, 8-BM, and 7-BM beamlines of the National Synchrotron Light Source II, U.S. DOE Office of Science User Facilities, operated for the DOE Office of Science by Brookhaven National Laboratory. Chaoshan Wu, Z.F. and Y. Y. are supported by the U.S. DOE's Office of EERE under the Vehicle Technologies Program under contract no. DE-EE0008864. This work made use of the shared facilities of the UC Santa Barbara MRSEC (DMR 720256), a member of the Materials Research Facilities Network (<http://www.mrfn.org>). This research used the Electron Microscopy facility of the Center for Functional Nanomaterials (CFN), which is a U.S. DOE Office of Science User Facility, at Brookhaven National Laboratory under Contract No. DE-SC0012704. Canhui Wang and Chao Wang were supported by the Advanced Research Projects

Agency-Energy, U.S. DOE, under Contract No. DE-AR0001191. FIB and SEM characterizations were performed at the San Diego Nanotechnology Infrastructure (SDNI) of UCSD supported by the NSF (Grant ECCS1542148). Raman facilities were supported by NSF through UCSD MRSEC, Grant No. DMR-201192. The authors acknowledge the use of facilities and instrumentation at the UC Irvine (UCI) Materials Research Institute (IMRI), which was supported in part by the NSF through the UCI MRSEC (DMR-2011967). XPS facilities was funded in part by the NSF Major Research Instrumentation. We thank the Molecular Mass Spectrometry Facility at UC San Diego for performing the MALDI-TOFMS measurement, which is supported by the NSF under Grant No. CHE-1338173.

Author contributions

J.Z. and P.L. conceptualized the idea and designed all of the experiments. S.P.O. and M.L.H.C. performed the theoretical calculations and drafted the results. S.T. and E.H. conducted the XAS and X-ray PDF tests. S.W. preformed the Raman, DSC, cryo-SEM and XPS measurements. Chaoshan Wu, Z.F. and Y.Y. collected the cross-sectional SEM images of the full cells at different states, including anode interfaces and cathode interfaces. H.N. collected EPR data, H.N. and R.J.C. analyzed and wrote up the results. Canhui Wang and Chao Wang performed the cryo-TEM. Y.X. and E.F. performed the XRD tests. Q.R.S.M. did the in-situ heating XRD test. H.L., S.Y., G.H., John Holoubek, Junghwa Hong, and C.S. helped with the synthesis of materials, cells fabrications, electrochemical performance tests, data analysis, discussion and revision. C.J.B. helped with the revised manuscript preparation and discussion. J.Z., P.L. and S.P.O. drafted the manuscript with input and revision from all authors. P.L. and S.P.O. supervised the research. J.Z and M.L.H.C contribute equally to this work.

Competing interests

P.L. and J.Z. report a US provisional patent application filed on February 13, 2023, Serial No. 63/484,659, based on this work.

Additional information

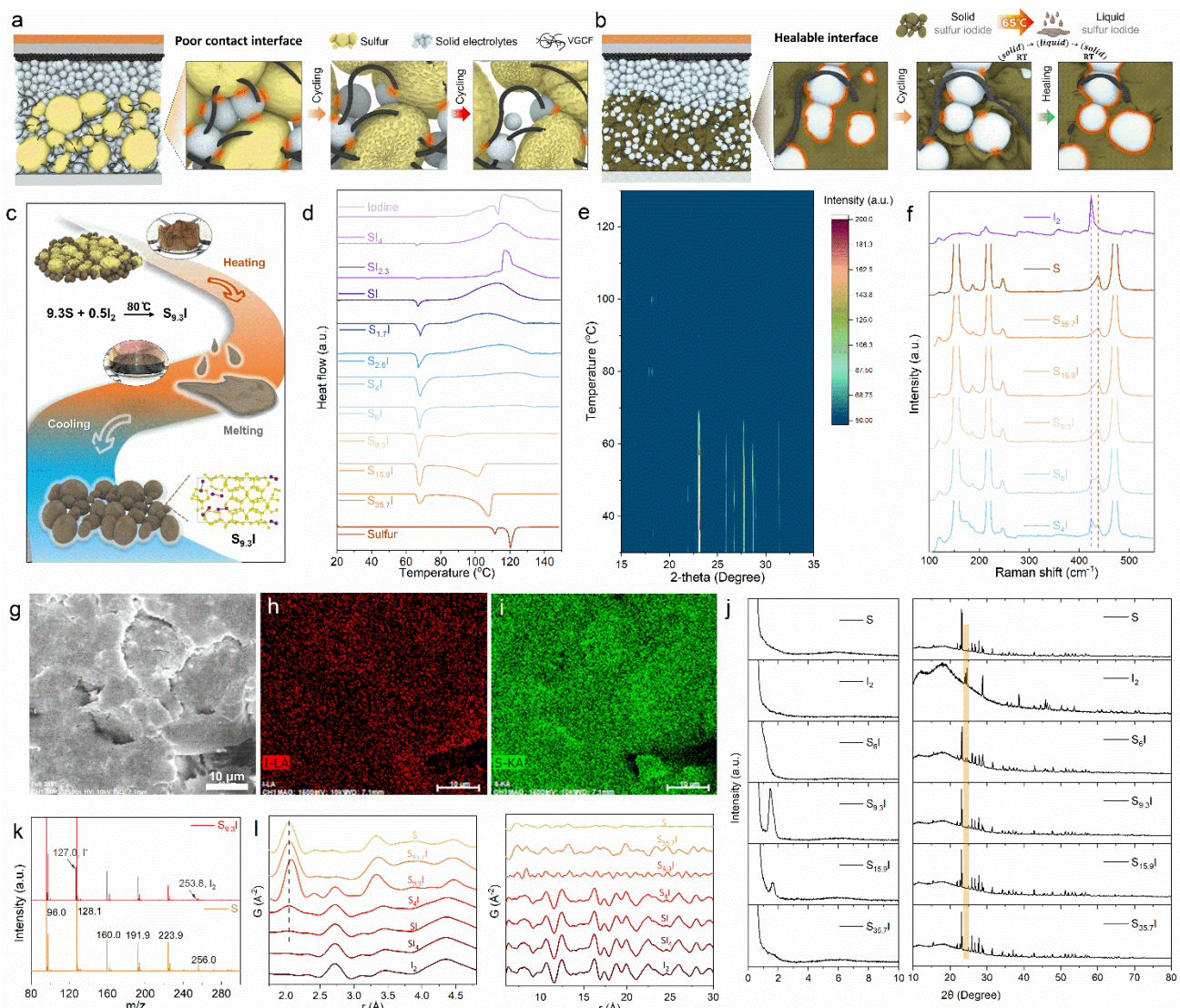
Supplementary information is available for this paper at <http://www.nature.com/supplementary-information>.

Correspondence and requests for materials should be addressed to S.P.O. or P.L.

Peer review information *Nature* thanks the anonymous reviewer(s) for their contribution to the peer review of this work.

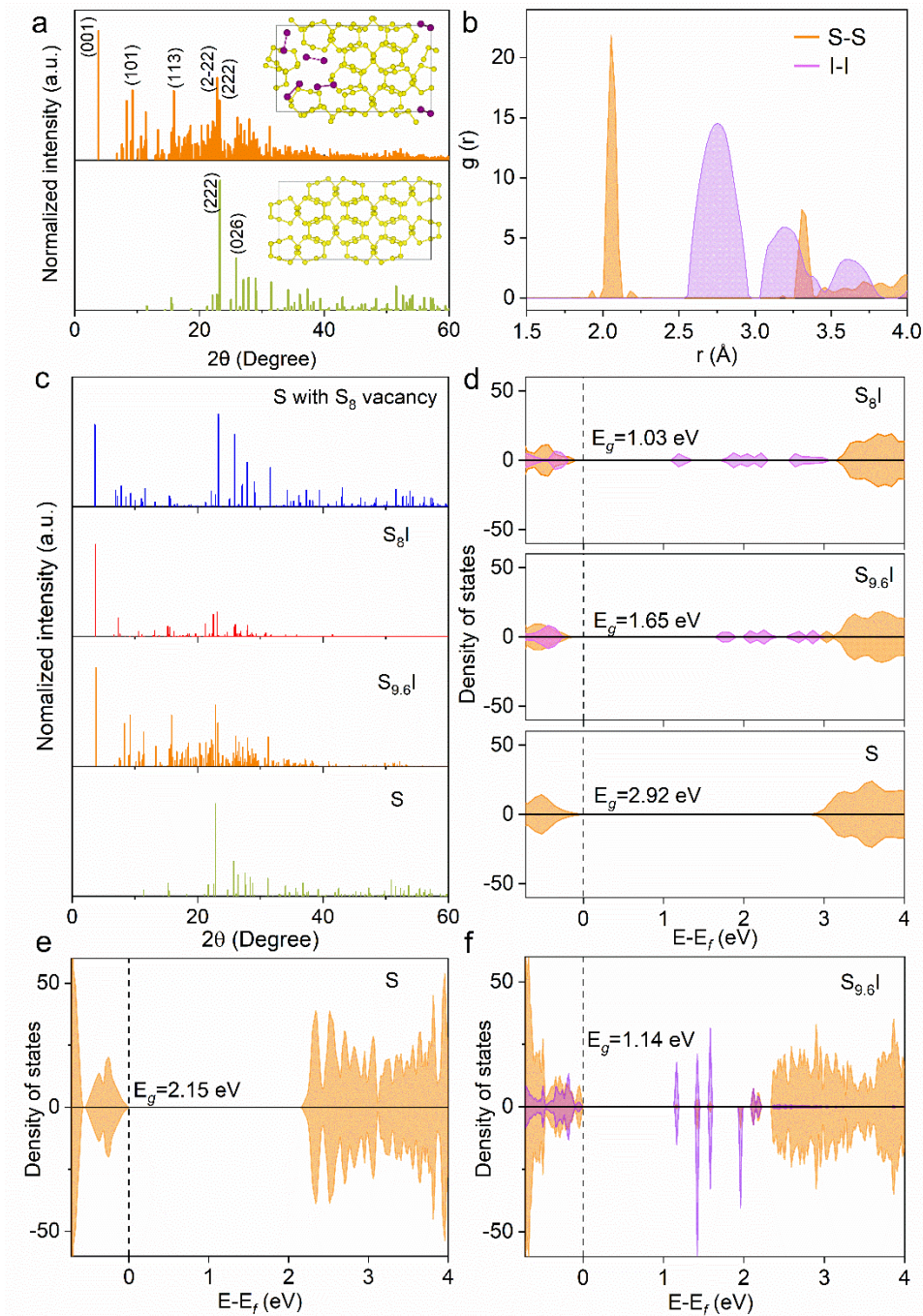
Reprints and permissions information is available at <http://www.nature.com/reprints>.

Extended data figures

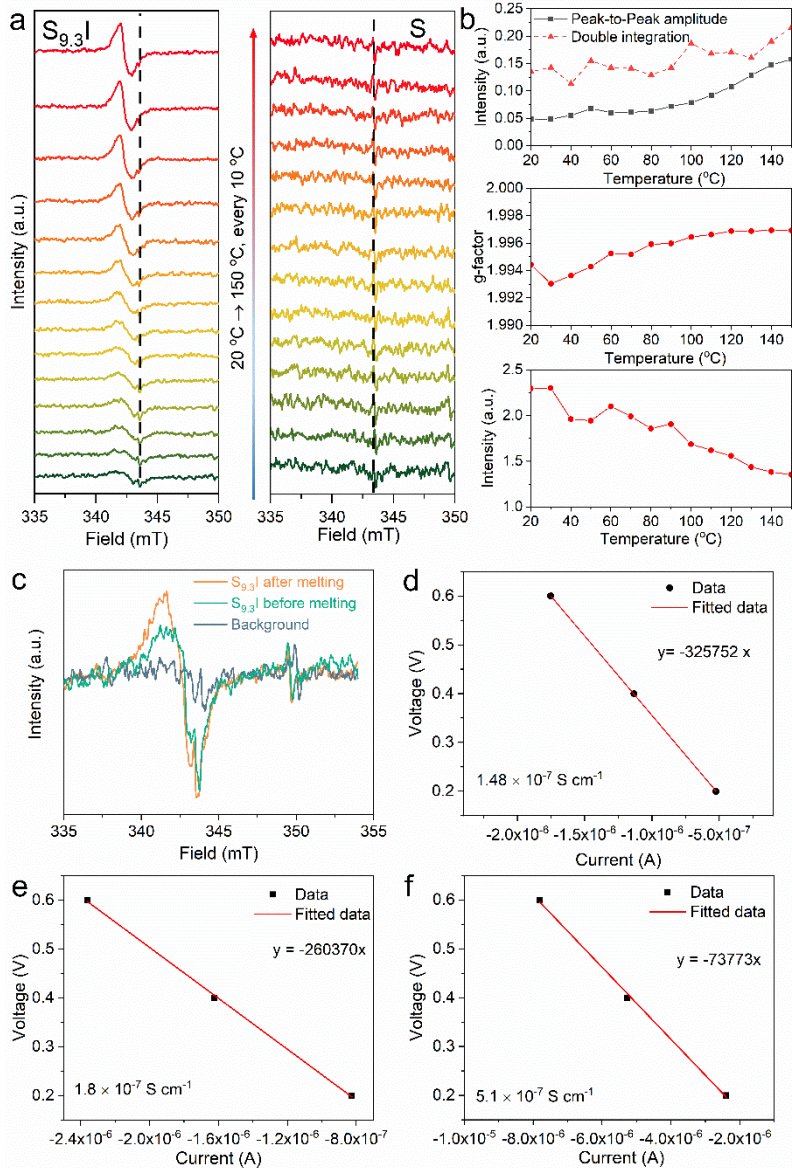


Extended data Fig. 1| Healable interfaces in SSLSBs with a low-melting-point sulfur iodide, and

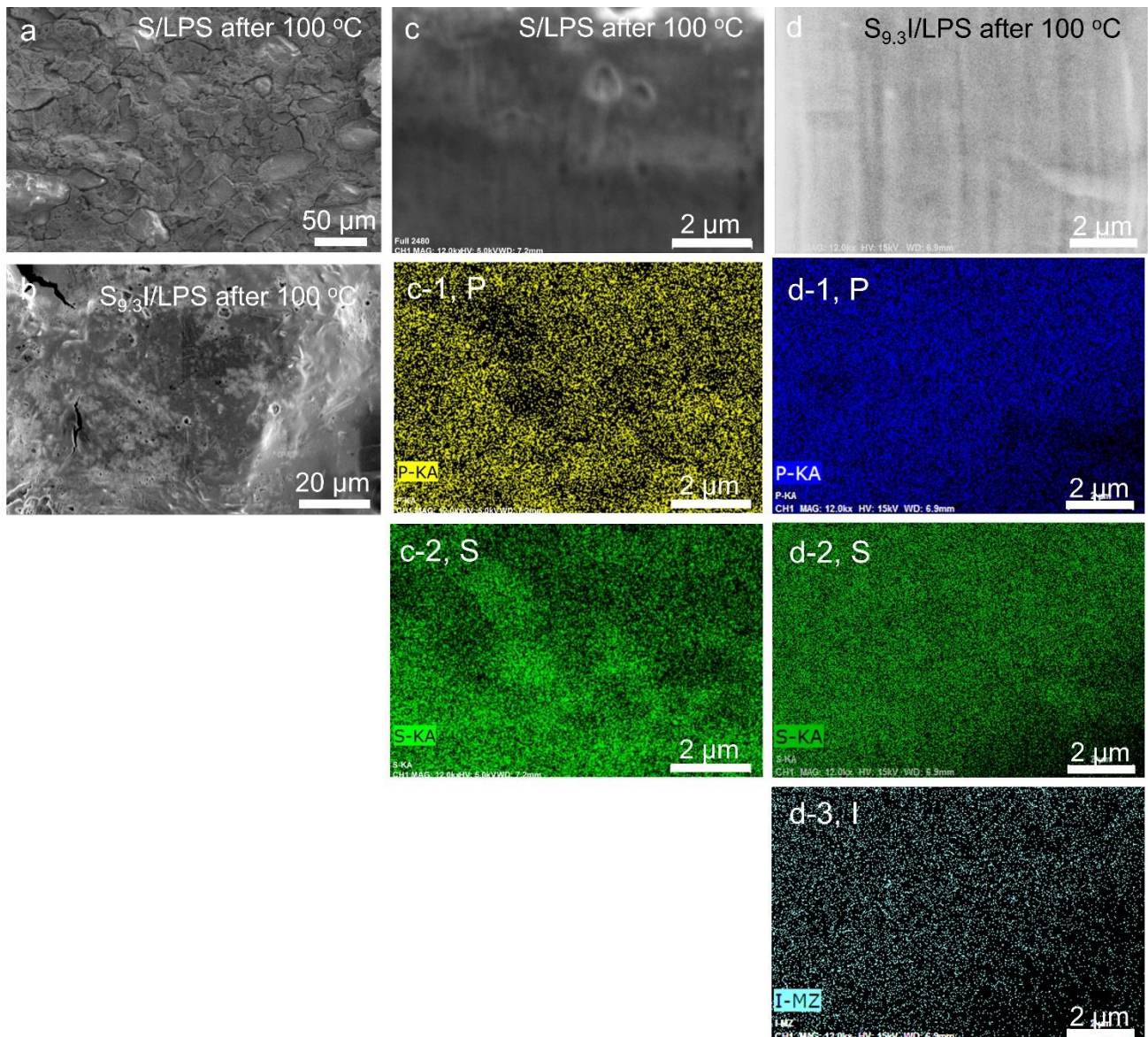
the synthesis and characterization of sulfur iodide materials. (a) Schematic of a solid state battery with elemental sulfur as the active material. Poor solid/solid contact develops during cycling due to volume changes of the active material. (b) Schematic of a solid state battery with sulfur iodide as the active material. Ideal active material/electrolyte interface is achieved through periodical heating to melt the cathode, thus healing the interface. (c) Illustration of the procedure to prepare $S_{9.3}I$. (d) The DSC curves of sulfur iodide with different S:I ratios in the temperature window of 20-150 °C. With S:I ratios decreasing from 1:0 to 9.3:1, the typical sulfur endothermic peak gradually disappears to transition to one phase melting behavior. Beyond 6:1, the exothermic peaks assigned to iodine are observed. (e) Spectra obtained during in-situ heating XRD of $S_{9.3}I$ from 30 to 130 °C with an 5 °C interval. (f) Raman spectra of sulfur iodide with different ratios, which features an iodine peak located at 423.8 cm^{-1} when the S:I ratio is less than 9.3:1. The cryo-SEM image (g) and the corresponding EDX mapping images of I (h) and S (i) element distribution of $S_{9.3}I$ after melting. (j) XRD of S, I_2 , $S_{35.7}I$, $S_{15.9}I$, $S_{9.3}I$, S_6I . In the low angle range, the relative intensity of the broadened peak centered at $\sim 1.5^\circ$ gradually increases with the increase of iodine, but from 9.3:1 to 6:1, the iodine diffraction peaks also emerge. (k) Mass spectra of S and $S_{9.3}I$. Compared to S, $S_{9.3}I$ shows two additional peaks centered at 127.0 and 253.8 m/z, which are attributed to I^- and I_2 species respectively. No peaks can be indexed to species containing S-I bonds. (l) The PDF of sulfur iodide materials after melting with different S and I ratios, elemental sulfur and iodine. When the ratio of S to I is below 9.3:1, bulk I_2 is present as indicated by the signals from the short and long range structures.



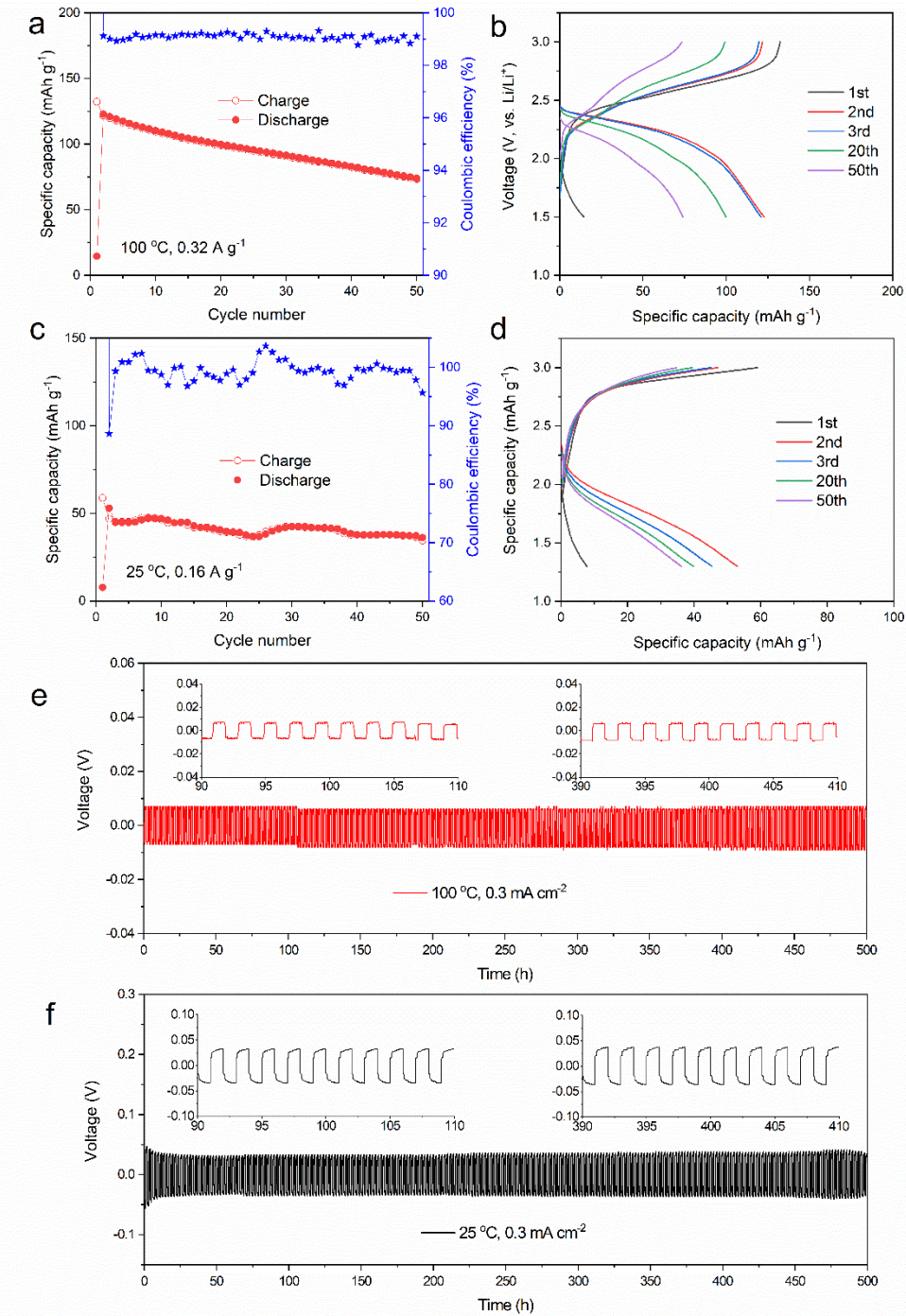
Extended data Fig. 2| Computed Crystal and electronic structure of S-I compounds. (a) Computed XRD patterns of elemental S and predicted $S_{9.6}I$ structure. (b) Computed PDF of $S_{9.6}I$. We attribute any minor discrepancies to the fact that the DFT relaxations are carried out at 0 K, while the experimental data is obtained at 300 K. (c) Computed XRD patterns of S, $S_{9.6}I$, S_8I and S with S_8 ring vacancy structure. (d) HSE projected density of states of S, $S_{9.6}I$ and S_8I . Elemental projected density of states for S (e) and $S_{9.6}I$ (f) using SCAN functionals.



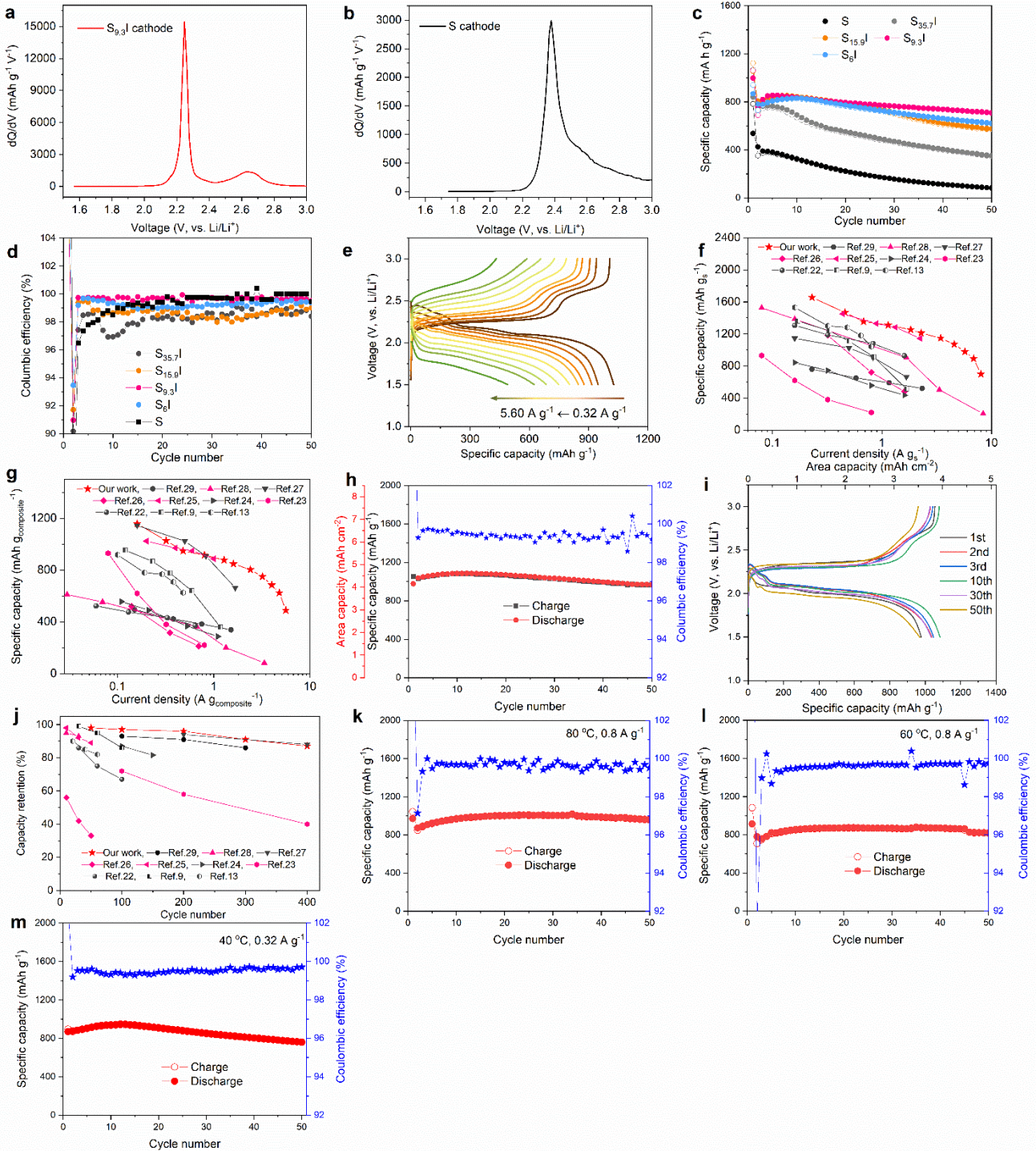
Extended data Fig. 3| Electronic structure and conductivities of sulfur iodide materials. (a) Variable temperature X-band EPR spectra collected on S_{9.3}I and elemental sulfur. The radical concentration in S_{9.3}I grows with increasing temperature, but not in S. (b) Temperature evolution of the EPR signal intensity (top panel), linewidth (middle panel), and g-factor (bottom panel) of S_{9.3}I. The g-factor for S_{9.3}I is approximately 1.99 and does not change appreciably with increasing temperature (bottom panel), suggesting that similar radical species are produced over the entire temperature range. (c) EPR spectra collected at 100 K on S_{9.3}I before and after melting. The electronic conductivity of S_{35.7}I (d), S_{15.9}I (e), and S₆I (f) measured by using a potentiostatic test at room temperature.



Extended data Fig. 4| SEM and elemental mapping of S and $S_{9.3}I$ mixed with LPS after heating at 100 °C. The SEM image of S/LPS mixture (a) and $S_{9.3}I$ /LPS mixture (b) after milling and heating at 100 °C. (c) The cross sectional cryo-FIB SEM images and corresponding element distribution images of S/LPS for S and P. The distribution of S and P is inhomogeneous. (d) Distribution of S, P, and I in $S_{9.3}I$ /LPS. The distribution in the entire area is homogeneous.

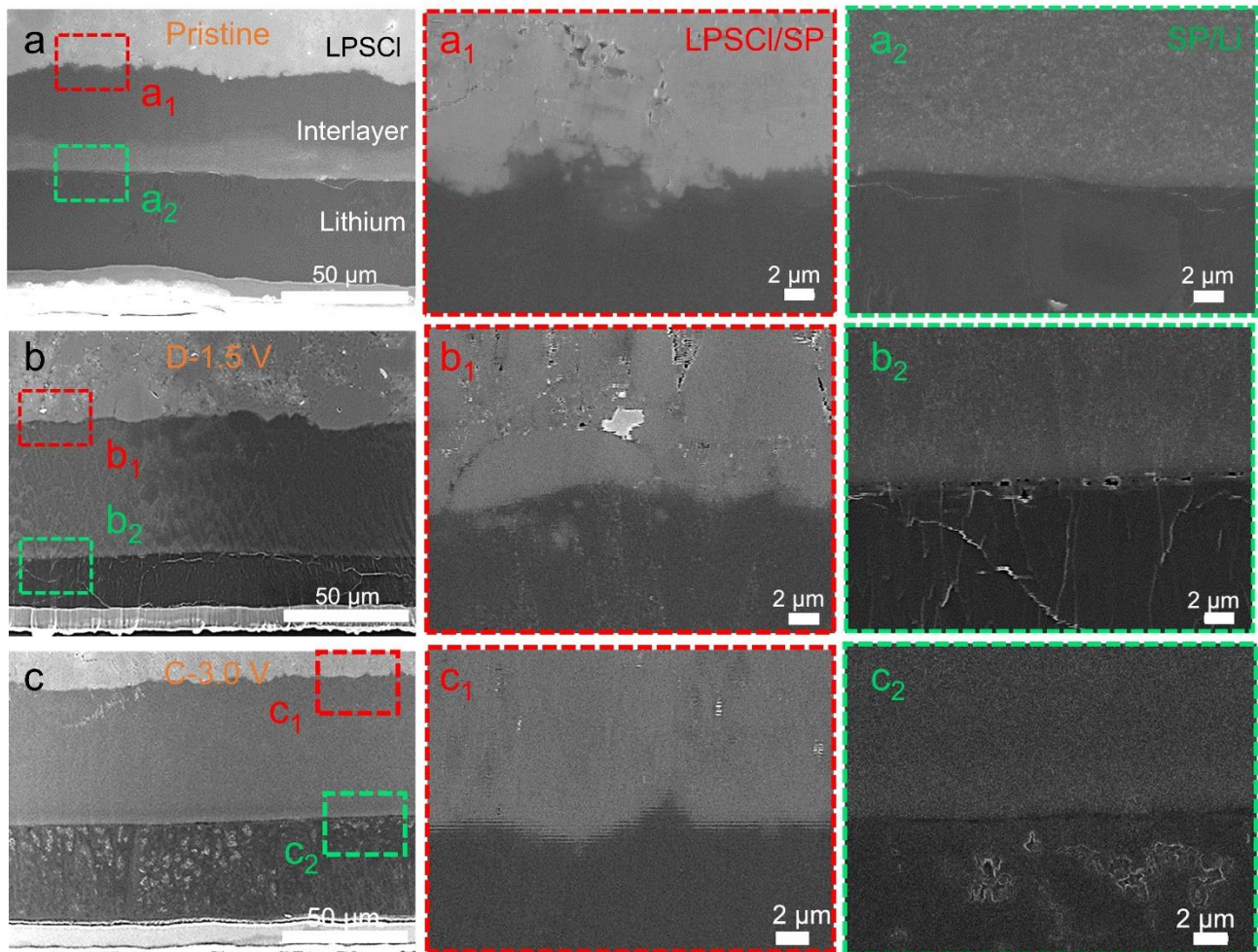


Extended data Fig. 5| Electrochemical performance data of solid state cell components. The cycling stability and capacity of a LPS/VGCF cathode at 100 °C (a) and 25 °C (c). The corresponding voltage profiles at 100 °C (b) and at 25 °C (d). Capacity contribution of LPS is very limited and the cycling stability of LPS is very poor either at 100 °C or 25 °C with low coulombic efficiencies. The long-term cycling stability of Li/SP/LPSCl/SP/Li symmetric cells at 100 °C (e) and 25 °C (f) at a current density of 0.3 mA cm⁻².

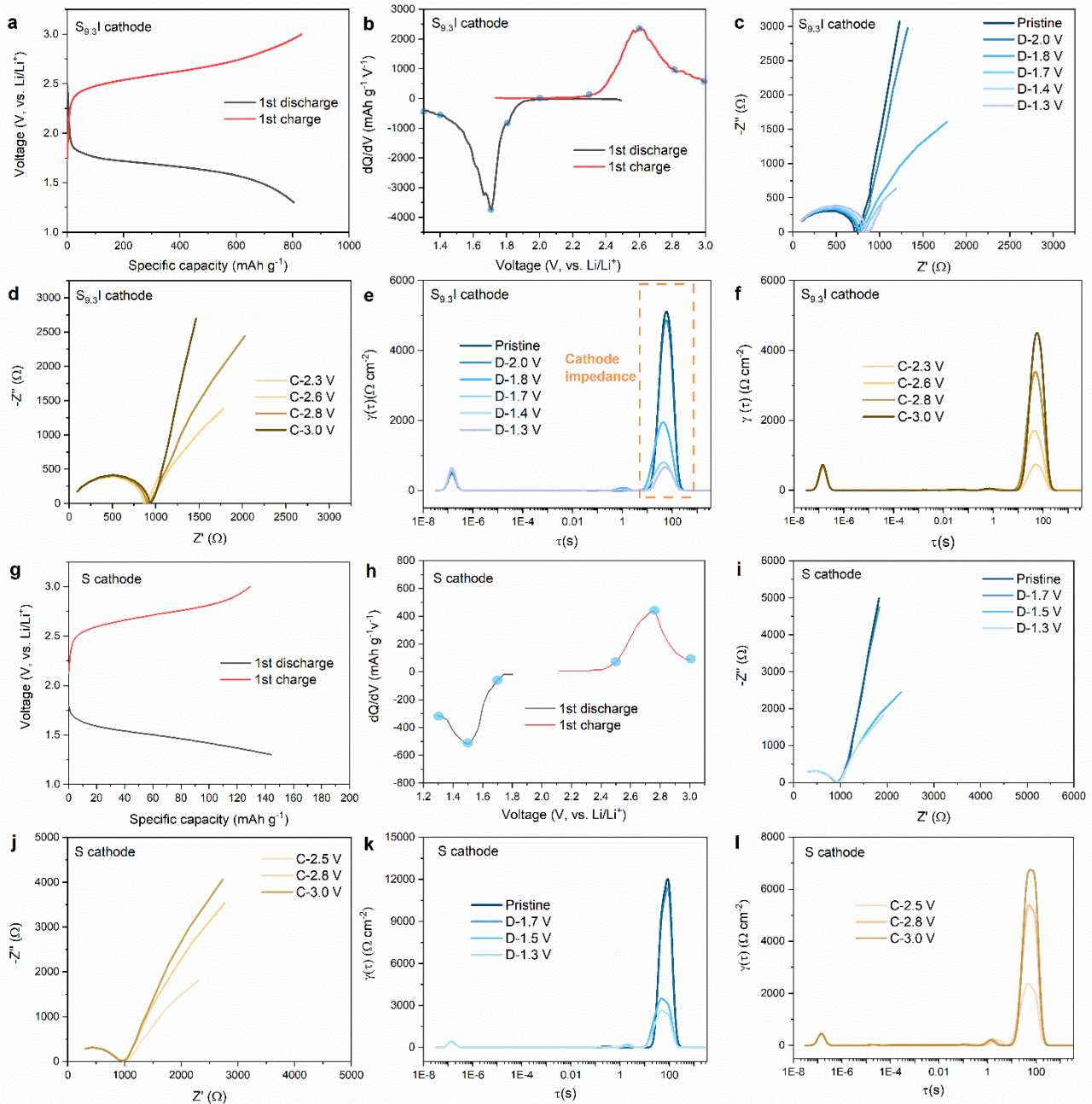


Extended Fig. 6| The performance of sulfur iodide cathode at different conditions and their comparison with other SSLSBs. The dQ/dV curves during delithiation of S_{9.3}I (a) and S (b) cathode based on the charging curves at 100 °C from Fig. 2a and 2b. (c) The cycling stability of S, S_{35.7}I, S_{15.9}I, S_{9.3}I and S₆I cathode at 1.6 A g⁻¹ and at 100 °C. (d) The corresponding cycling coulombic efficiency in (c). (e) Rate capability of S_{9.3}I cathode at 100 °C at current densities of 0.32, 0.48, 0.80, 1.28, 1.60, 2.00, 2.40, 2.80, 3.20, 3.60, 4.00, 4.40, 4.80, 5.20, 5.60, 6.00, 6.40, 6.80, 7.20, 7.60, 8.00, 8.40, 8.80, 9.20, 9.60, 10.00, 10.40, 10.80, 11.20, 11.60, 12.00, 12.40, 12.80, 13.20, 13.60, 14.00, 14.40, 14.80, 15.20, 15.60, 16.00, 16.40, 16.80, 17.20, 17.60, 18.00, 18.40, 18.80, 19.20, 19.60, 20.00, 20.40, 20.80, 21.20, 21.60, 22.00, 22.40, 22.80, 23.20, 23.60, 24.00, 24.40, 24.80, 25.20, 25.60, 26.00, 26.40, 26.80, 27.20, 27.60, 28.00, 28.40, 28.80, 29.20, 29.60, 30.00, 30.40, 30.80, 31.20, 31.60, 32.00, 32.40, 32.80, 33.20, 33.60, 34.00, 34.40, 34.80, 35.20, 35.60, 36.00, 36.40, 36.80, 37.20, 37.60, 38.00, 38.40, 38.80, 39.20, 39.60, 40.00, 40.40, 40.80, 41.20, 41.60, 42.00, 42.40, 42.80, 43.20, 43.60, 44.00, 44.40, 44.80, 45.20, 45.60, 46.00, 46.40, 46.80, 47.20, 47.60, 48.00, 48.40, 48.80, 49.20, 49.60, 50.00, 50.40, 50.80, 51.20, 51.60, 52.00, 52.40, 52.80, 53.20, 53.60, 54.00, 54.40, 54.80, 55.20, 55.60, 56.00, 56.40, 56.80, 57.20, 57.60, 58.00, 58.40, 58.80, 59.20, 59.60, 60.00, 60.40, 60.80, 61.20, 61.60, 62.00, 62.40, 62.80, 63.20, 63.60, 64.00, 64.40, 64.80, 65.20, 65.60, 66.00, 66.40, 66.80, 67.20, 67.60, 68.00, 68.40, 68.80, 69.20, 69.60, 70.00, 70.40, 70.80, 71.20, 71.60, 72.00, 72.40, 72.80, 73.20, 73.60, 74.00, 74.40, 74.80, 75.20, 75.60, 76.00, 76.40, 76.80, 77.20, 77.60, 78.00, 78.40, 78.80, 79.20, 79.60, 80.00, 80.40, 80.80, 81.20, 81.60, 82.00, 82.40, 82.80, 83.20, 83.60, 84.00, 84.40, 84.80, 85.20, 85.60, 86.00, 86.40, 86.80, 87.20, 87.60, 88.00, 88.40, 88.80, 89.20, 89.60, 90.00, 90.40, 90.80, 91.20, 91.60, 92.00, 92.40, 92.80, 93.20, 93.60, 94.00, 94.40, 94.80, 95.20, 95.60, 96.00, 96.40, 96.80, 97.20, 97.60, 98.00, 98.40, 98.80, 99.20, 99.60, 100.00, 100.40, 100.80, 101.20, 101.60, 102.00, 102.40, 102.80, 103.20, 103.60, 104.00, 104.40, 104.80, 105.20, 105.60, 106.00, 106.40, 106.80, 107.20, 107.60, 108.00, 108.40, 108.80, 109.20, 109.60, 110.00, 110.40, 110.80, 111.20, 111.60, 112.00, 112.40, 112.80, 113.20, 113.60, 114.00, 114.40, 114.80, 115.20, 115.60, 116.00, 116.40, 116.80, 117.20, 117.60, 118.00, 118.40, 118.80, 119.20, 119.60, 120.00, 120.40, 120.80, 121.20, 121.60, 122.00, 122.40, 122.80, 123.20, 123.60, 124.00, 124.40, 124.80, 125.20, 125.60, 126.00, 126.40, 126.80, 127.20, 127.60, 128.00, 128.40, 128.80, 129.20, 129.60, 130.00, 130.40, 130.80, 131.20, 131.60, 132.00, 132.40, 132.80, 133.20, 133.60, 134.00, 134.40, 134.80, 135.20, 135.60, 136.00, 136.40, 136.80, 137.20, 137.60, 138.00, 138.40, 138.80, 139.20, 139.60, 140.00, 140.40, 140.80, 141.20, 141.60, 142.00, 142.40, 142.80, 143.20, 143.60, 144.00, 144.40, 144.80, 145.20, 145.60, 146.00, 146.40, 146.80, 147.20, 147.60, 148.00, 148.40, 148.80, 149.20, 149.60, 150.00, 150.40, 150.80, 151.20, 151.60, 152.00, 152.40, 152.80, 153.20, 153.60, 154.00, 154.40, 154.80, 155.20, 155.60, 156.00, 156.40, 156.80, 157.20, 157.60, 158.00, 158.40, 158.80, 159.20, 159.60, 160.00, 160.40, 160.80, 161.20, 161.60, 162.00, 162.40, 162.80, 163.20, 163.60, 164.00, 164.40, 164.80, 165.20, 165.60, 166.00, 166.40, 166.80, 167.20, 167.60, 168.00, 168.40, 168.80, 169.20, 169.60, 170.00, 170.40, 170.80, 171.20, 171.60, 172.00, 172.40, 172.80, 173.20, 173.60, 174.00, 174.40, 174.80, 175.20, 175.60, 176.00, 176.40, 176.80, 177.20, 177.60, 178.00, 178.40, 178.80, 179.20, 179.60, 180.00, 180.40, 180.80, 181.20, 181.60, 182.00, 182.40, 182.80, 183.20, 183.60, 184.00, 184.40, 184.80, 185.20, 185.60, 186.00, 186.40, 186.80, 187.20, 187.60, 188.00, 188.40, 188.80, 189.20, 189.60, 190.00, 190.40, 190.80, 191.20, 191.60, 192.00, 192.40, 192.80, 193.20, 193.60, 194.00, 194.40, 194.80, 195.20, 195.60, 196.00, 196.40, 196.80, 197.20, 197.60, 198.00, 198.40, 198.80, 199.20, 199.60, 200.00, 200.40, 200.80, 201.20, 201.60, 202.00, 202.40, 202.80, 203.20, 203.60, 204.00, 204.40, 204.80, 205.20, 205.60, 206.00, 206.40, 206.80, 207.20, 207.60, 208.00, 208.40, 208.80, 209.20, 209.60, 210.00, 210.40, 210.80, 211.20, 211.60, 212.00, 212.40, 212.80, 213.20, 213.60, 214.00, 214.40, 214.80, 215.20, 215.60, 216.00, 216.40, 216.80, 217.20, 217.60, 218.00, 218.40, 218.80, 219.20, 219.60, 220.00, 220.40, 220.80, 221.20, 221.60, 222.00, 222.40, 222.80, 223.20, 223.60, 224.00, 224.40, 224.80, 225.20, 225.60, 226.00, 226.40, 226.80, 227.20, 227.60, 228.00, 228.40, 228.80, 229.20, 229.60, 230.00, 230.40, 230.80, 231.20, 231.60, 232.00, 232.40, 232.80, 233.20, 233.60, 234.00, 234.40, 234.80, 235.20, 235.60, 236.00, 236.40, 236.80, 237.20, 237.60, 238.00, 238.40, 238.80, 239.20, 239.60, 240.00, 240.40, 240.80, 241.20, 241.60, 242.00, 242.40, 242.80, 243.20, 243.60, 244.00, 244.40, 244.80, 245.20, 245.60, 246.00, 246.40, 246.80, 247.20, 247.60, 248.00, 248.40, 248.80, 249.20, 249.60, 250.00, 250.40, 250.80, 251.20, 251.60, 252.00, 252.40, 252.80, 253.20, 253.60, 254.00, 254.40, 254.80, 255.20, 255.60, 256.00, 256.40, 256.80, 257.20, 257.60, 258.00, 258.40, 258.80, 259.20, 259.60, 260.00, 260.40, 260.80, 261.20, 261.60, 262.00, 262.40, 262.80, 263.20, 263.60, 264.00, 264.40, 264.80, 265.20, 265.60, 266.00, 266.40, 266.80, 267.20, 267.60, 268.00, 268.40, 268.80, 269.20, 269.60, 270.00, 270.40, 270.80, 271.20, 271.60, 272.00, 272.40, 272.80, 273.20, 273.60, 274.00, 274.40, 274.80, 275.20, 275.60, 276.00, 276.40, 276.80, 277.20, 277.60, 278.00, 278.40, 278.80, 279.20, 279.60, 280.00, 280.40, 280.80, 281.20, 281.60, 282.00, 282.40, 282.80, 283.20, 283.60, 284.00, 284.40, 284.80, 285.20, 285.60, 286.00, 286.40, 286.80, 287.20, 287.60, 288.00, 288.40, 288.80, 289.20, 289.60, 290.00, 290.40, 290.80, 291.20, 291.60, 292.00, 292.40, 292.80, 293.20, 293.60, 294.00, 294.40, 294.80, 295.20, 295.60, 296.00, 296.40, 296.80, 297.20, 297.60, 298.00, 298.40, 298.80, 299.20, 299.60, 300.00, 300.40, 300.80, 301.20, 301.60, 302.00, 302.40, 302.80, 303.20, 303.60, 304.00, 304.40, 304.80, 305.20, 305.60, 306.00, 306.40, 306.80, 307.20, 307.60, 308.00, 308.40, 308.80, 309.20, 309.60, 310.00, 310.40, 310.80, 311.20, 311.60, 312.00, 312.40, 312.80, 313.20, 313.60, 314.00, 314.40, 314.80, 315.20, 315.60, 316.00, 316.40, 316.80, 317.20, 317.60, 318.00, 318.40, 318.80, 319.20, 319.60, 320.00, 320.40, 320.80, 321.20, 321.60, 322.00, 322.40, 322.80, 323.20, 323.60, 324.00, 324.40, 324.80, 325.20, 325.60, 326.00, 326.40, 326.80, 327.20, 327.60, 328.00, 328.40, 328.80, 329.20, 329.60, 330.00, 330.40, 330.80, 331.20, 331.60, 332.00, 332.40, 332.80, 333.20, 333.60, 334.00, 334.40, 334.80, 335.20, 335.60, 336.00, 336.40, 336.80, 337.20, 337.60, 338.00, 338.40, 338.80, 339.20, 339.60, 340.00, 340.40, 340.80, 341.20, 341.60, 342.00, 342.40, 342.80, 343.20, 343.60, 344.00, 344.40, 344.80, 345.20, 345.60, 346.00, 346.40, 346.80, 347.20, 347.60, 348.00, 348.40, 348.80, 349.20, 349.60, 350.00, 350.40, 350.80, 351.20, 351.60, 352.00, 352.40, 352.80, 353.20, 353.60, 354.00, 354.40, 354.80, 355.20, 355.60, 356.00, 356.40, 356.80, 357.20, 357.60, 358.00, 358.40, 358.80, 359.20, 359.60, 360.00, 360.40, 360.80, 361.20, 361.60, 362.00, 362.40, 362.80, 363.20, 363.60, 364.00, 364.40, 364.80, 365.20, 365.60, 366.00, 366.40, 366.80, 367.20, 367.60, 368.00, 368.40, 368.80, 369.20, 369.60, 370.00, 370.40, 370.80, 371.20, 371.60, 372.00, 372.40, 372.80, 373.20, 373.60, 374.00, 374.40, 374.80, 375.20, 375.60, 376.00, 376.40, 376.80, 377.20, 377.60, 378.00, 378.40, 378.80, 379.20, 379.60, 380.00, 380.40, 380.80, 381.20, 381.60, 382.00, 382.40, 382.80, 383.20, 383.60, 384.00, 384.40, 384.80, 385.20, 385.60, 386.00, 386.40, 386.80, 387.20, 387.60, 388.00, 388.40, 388.80, 389.20, 389.60, 390.00, 390.40, 390.80, 391.20, 391.60, 392.00, 392.40, 392.80, 393.20, 393.60, 394.00, 394.40, 394.80, 395.20, 395.60, 396.00, 396.40, 396.80, 397.20, 397.60, 398.00, 398.40, 398.80, 399.20, 399.60, 400.00, 400.40, 400.80, 401.20, 401.60, 402.00, 402.40, 402.80, 403.20, 403.60, 404.00, 404.40, 404.80, 405.20, 405.60, 406.00, 406.40, 406.80, 407.20, 407.60, 408.00, 408.40, 408.80, 409.20, 409.60, 410.00, 410.40, 410.80, 411.20, 411.60, 412.00, 412.40, 412.80, 413.20, 413.60, 414.00, 414.40, 414.80, 415.20, 415.60, 416.00, 416.40, 416.80, 417.20, 417.60, 418.00, 418.40, 418.80, 419.20, 419.60, 420.00, 420.40, 420.80, 421.20, 421.60, 422.00, 422.40, 422.80, 423.20, 423.60, 424.00, 424.40, 424.80, 425.20, 425.60, 426.00, 426.40, 426.80, 427.20, 427.60, 428.00, 428.40, 428.80, 429.20, 429.60, 430.00, 430.40, 430.80, 431.20, 431.60, 432.00, 432.40, 432.80, 433.20, 433.60, 434.00, 434.40, 434.80, 435.20, 435.60, 436.00, 436.40, 436.80, 437.20, 437.60, 438.00, 438.40, 438.80, 439.20, 439.60, 440.00, 440.40, 440.80, 441.20, 441.60, 442.00, 442.40, 442.80, 443.20, 443.60, 444.00, 444.40, 444.80, 445.20, 445.60, 446.00, 446.40, 446.80, 447.20, 447.60, 448.00, 448.40, 448.80, 449.20, 449.60, 450.00, 450.40, 450.80, 451.20, 451.60, 452.00, 452.40, 452.80, 453.20, 453.60, 454.00, 454.40, 454.80, 455.20, 455.60, 456.00, 456.40, 456.80, 457.20, 457.60, 458.00, 458.40, 458.80, 459.20, 459.60, 460.00, 460.40, 460.80, 461.20, 461.60, 462.00, 462.40, 462.80, 463.20, 463.60, 464.00, 464.40, 464.80, 465.20, 465.60, 466.00, 466.40, 466.80, 467.20, 467.60, 468.00, 468.40, 468.80, 469.20, 469.60, 470.00, 470.40, 470.80, 471.20, 471.60, 472.00, 472.40, 472.80, 473.20, 473.60, 474.00, 474.40, 474.80, 475.20, 475.60, 476.00, 476.40, 476.80, 477.20, 477.60, 478.00, 478.40, 478.80, 479.20, 479.60, 480.00, 480.40, 480.80, 481.20, 481.60, 482.00, 482.40, 482.80, 483.20, 483.60, 484.00, 484.40, 484.80, 485.20, 485.60, 486.00, 486.40, 486.80, 487.20, 487.60, 488.00, 488.40, 488.80, 489.20, 489.60, 490.00, 490.40, 490.80, 491.20, 491.60, 492.00, 492.40, 492.80, 493.20, 493.60, 494.00, 494.40, 494.80, 495.20, 495.60, 496.00, 496.40, 496.80, 497.20, 497.60, 498.00, 498.40, 498.80, 499.20, 499.60, 500.00, 500.40, 500.80, 501.20, 501.60, 502.00, 502.40, 502.80, 503.20, 503.60, 504.00, 504.40, 504.80, 505.20, 505.60, 506.00, 506.40, 506.80, 507.20, 507.60, 508.00, 508.40, 508.80, 509.20, 509.60, 510.00, 510.40, 510.80, 511.20, 511.60, 512.00, 512.40, 512.80, 513.20, 513.60, 514.00, 514.40,

2.40, 3.20, 4.00, 4.80 and 5.60 A g⁻¹. Rate performance comparison between Li-S_{9.3}I solid state batteries with other SSLSBs: based on the weight of (f) only S and (g) S composite, red-colored symbols represent Li metal anode based SSLSBs while other cells used non-Li metal anodes. (h) The cycling performance of S_{9.3}I cathode with a high mass loading of 4.2 mg cm⁻² at 0.32 A g⁻¹ and at 100 °C. (i) The corresponding voltage profiles at different cycles in (h). (j) Cycling stability comparison between Li-S_{9.3}I solid state batteries with other SSLSBs. The cycling performance of the S_{9.3}I cathode at varied temperatures and current densities: (k) 80 °C, 0.8 A g⁻¹, (l) 60 °C, 0.8 A g⁻¹, (m) 40 °C, 0.32 A g⁻¹. It should be noted that a low current density is applied to the cells tested at all temperatures during the initial formation cycle.

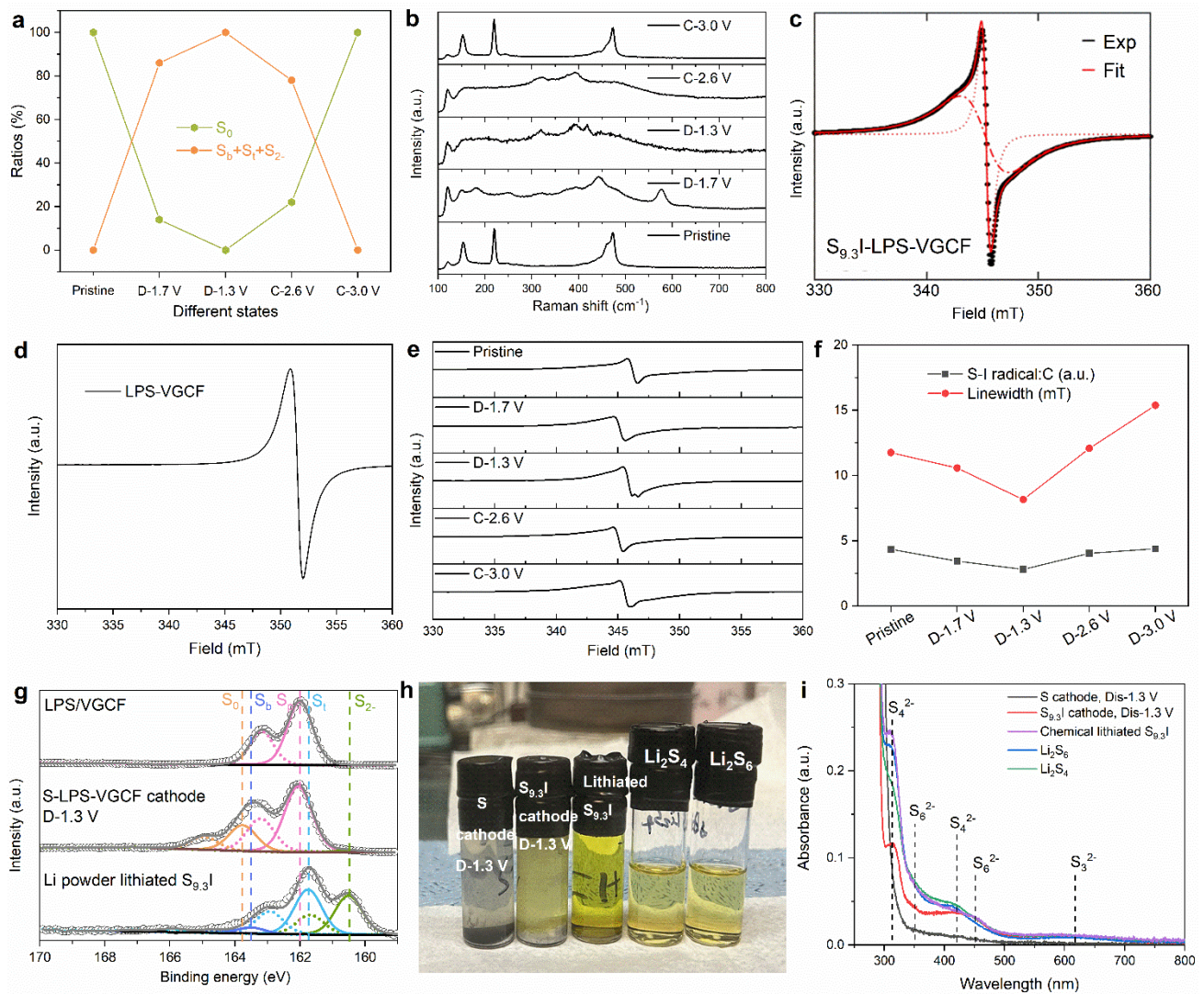


Extended data Fig. 7| Morphological study of the Li-SP-LPSCI interface during cycling in full cells. The cross-sectional SEM of Li/SP/LPSCI interface at different states: pristine (a), fully discharged to 1.5 V (b) and fully charged back to 3.0 V (c). It should be noted that all of the anode interfaces were cut from the full cells with the configuration of $S_{9.3}I$ -LPS-VGCF/LPS/LPSCI/SP/Li with a high mass loading of $S_{9.3}I$ 4.2 mg cm^{-2} running at 100°C and at a current density of 0.32 A g^{-1} . At the pristine state (a), both the Li/SP interface and SP/LPSCI SSE interface are well connected. After discharge (b), the thickness of Li decreases from $\sim 50 \text{ }\mu\text{m}$ to $\sim 30 \text{ }\mu\text{m}$, the $20 \text{ }\mu\text{m}$ difference corresponding to an area capacity of $\sim 4.0 \text{ mAh cm}^{-2}$. After charging back to 3.0 V (c), the thickness of Li recovers back to $\sim 50 \text{ }\mu\text{m}$. Importantly, both the Li/SP interface and SP/LPSCI SSE interface are well maintained without the growth of Li dendrites during the discharge and charge processes.



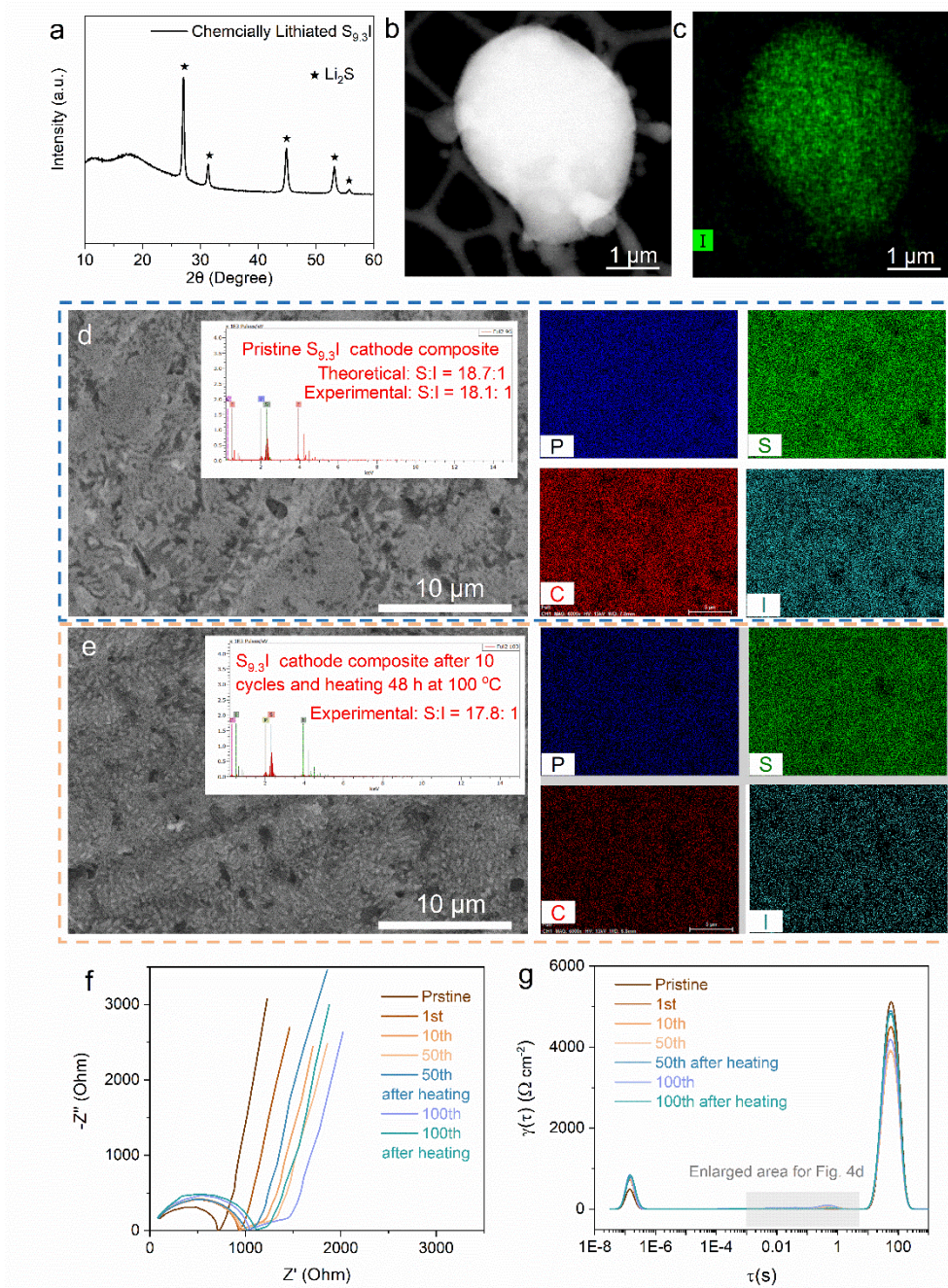
Extended Fig. 8| EIS study of Li-S_{9.3}I and Li-S full cell at 25 °C during initial cycles. (a) The initial discharge/charge curves of a Li-S_{9.3}I cell, and the corresponding dQ/dV curves (b) derive from (a). (c) The EIS of the Li-S_{9.3}I cell at different states of discharge. (d) The EIS of the Li-S_{9.3}I cell at different states of charge. The DRT analysis of EIS at different states of discharge (e) related to (c), and states of charge (f) related to (d). (g) The initial discharge/charge curves of a Li-S cathode, and the corresponding dQ/dV curves (h) derive from (g). (i) The EIS of the Li-S cell at different states of discharge. (j) The EIS of the Li-S cell at different states of charge. The DRT analysis of EIS at different

states of discharge (k) related to (i), and states of charge (l) related to (j). The impedance of $S_{9.3}I$ cathode is much lower than that of pure S cathode during cycling.



Extended data Fig. 9 | Characterizations of intermediates during cycling to diagnose the S_{9.3}I cathode working mechanism. (a) The corresponding ratios of S₀, S_b, S_t, and S₂₋ in the S_{9.3}I cathode in Fig. 3b at different discharge/charge states. (b) Ex-situ Raman spectra of S_{9.3}I during the discharge/charge processes. The ex-situ Raman spectra suggest the good reversibility of S_{9.3}I cathode at RT. X-band EPR spectra obtained on (c) the pristine S_{9.3}I cathode, and on (d) the SSE and carbon mixture (LPS-VGCF). (e) Ex-situ EPR data obtained on cathode samples harvested from cells stopped at various stages of the initial discharge/charge process. (f) Parameters obtained from fits of the EPR spectra in (e), including the ratios of the signal intensities from the S_{9.3}I cathode material and from the VGCF additive, and the linewidth of the S_{9.3}I EPR signal. The ratio of S_{9.3}I radicals to carbon decreases during initial discharge and grows upon subsequent charge (f). This trend is consistent with the

following model, assuming that polysulfide chains that form in the solid-state exist as dianions and cannot be detected in our EPR measurements, unlike EPR-active polysulfide radicals formed in solution through disproportionation of polysulfide dianions (as in conventional Li-S cells). (g) The S_{2p} high resolution XPS of comparison samples, including LPS/VGCF mixture, S cathode discharge to 1.3 V (D-1.3 V) and chemically lithiated $S_{9.3}I$ prepared by reacting with Li powder with an equivalent capacity of ~ 800 mAh g $^{-1}$. (h) Digital photos of elemental S cathode discharged to 1.3 V, $S_{9.3}I$ cathode discharged to 1.3 V, chemically lithiated $S_{9.3}I$ immersed in THF solution and standard Li_2S_4 , Li_2S_6 THF solutions. (i) The UV-Vis spectra of corresponding samples in (h). The $S_{9.3}I$ cathode discharged to 1.3 V and chemically lithiated $S_{9.3}I$ suspensions exhibit the color of LiS_x solutions immediately, but elemental S cathode discharged to 1.3 V doesn't show any change.



Extended data Fig. 10| Structure and property evolution of $\text{S}_{9.3}\text{I}$ cathode during cycling. (a) XRD of chemically lithiated $\text{S}_{9.3}\text{I}$. A chemically lithiated $\text{S}_{9.3}\text{I}$ particle with a few micrometers (b) and corresponding iodine element mapping (c) shows a uniform iodine distribution. EDX mapping images of $\text{S}_{9.3}\text{I}$ cathode at different states: (d) Pristine, (e) after 10 cycles and heated over 48 hours at 100 °C, and the corresponding element analysis. There is only a very small S: I atomic ratio change after 10 cycles and then heated at 100 °C for over 48 h, indicating the thermal stability of $\text{S}_{9.3}\text{I}$ cathode. (f) EIS spectra and (g) corresponding DRT analysis of Li- $\text{S}_{9.3}\text{I}$ full cell at different cycles.

Extended data Table 1| Comparison of experimental bulk S₈ cell parameters with PBE, optB88 and SCAN computed values. The percentage errors with respect to experimental value are provided in parentheses.

Cell parameter	Experimental	PBE	Optb88	SCAN
a (Å)	10.474	11.528 (10.06%)	10.333 (-1.34%)	10.587 (1.08%)
b (Å)	12.881	13.802 (7.15%)	12.829 (-0.40%)	12.952 (0.552%)
c (Å)	24.491	25.822 (5.43%)	24.509 (0.048%)	24.567 (0.313%)

Extended data Table 2| Comparison of cycling stability and rate capacities of S_{9.3}I and other previously reported high performance S composites cathodes in SSLSBs.

S composite active material	S ratio, wt%	SSE	Anode	Cycling stability	Capacity based on S at varied current densities	Capacity based on S composite at varied current densities
S@CNTs ⁹	70	LGPS	Li-Al alloy	100 cycles, 86.79%	1362, 1239, 1110, 914, and 514 mAh g ⁻¹ at 0.17, 0.33, 0.5, 0.84, and 1.67 A g ⁻¹	953.4, 867.3, 777, 639.8, 359.8 mAh g ⁻¹ at 0.12, 0.23, 0.35, 0.59 and 1.17 A g ⁻¹
S@C ¹³	60	LPSC	Li-Mg-Li ₅ B ₄ -AgC alloy	60 cycles, 82%	1530, 1300, 1280, 1180, 1042 mAh g ⁻¹ at 0.16, 0.32, 0.48, 0.64, and 0.8 A g ⁻¹	918, 780, 768, 708, 625.2 mAh g ⁻¹ at 0.1, 0.19, 0.29, 0.38, and 0.48 A g ⁻¹
SPAN ²²	40	PVDF-HFP-in-LiFSI	Li-In alloy	100 cycles, 67.7%,	1306.8, 1189.3, 1078.6, and 928.8 at 0.16, 0.32, 0.83, and 1.6 A g ⁻¹	522.7, 475.7, 431.4, 371.5 mAh g ⁻¹ at 0.06, 0.13, 0.33, and 0.64 A g ⁻¹
S ²³	100	LiDFT FSI/PEO	Li	72.6% at 100 th cycle, 58.1% at 200 th cycle, 40.3% at 400 th cycle	930, 620, 380, 220 mAh g ⁻¹ at 0.08, 0.16, 0.32, and 0.8 A g ⁻¹	930, 620, 380, 220 mAh g ⁻¹ at 0.08, 0.16, 0.32 and 0.8 A g ⁻¹
Se _{0.05} S _{0.95} @pPAN ²⁴	66	LGPS	Li-In alloy	150 cycles, 81.6%, 0.16 A g ⁻¹	842.2, 742.9, 555.7 and 434.6 mAh g ⁻¹ at 0.16, 0.32, 0.8 and 1.6 A g ⁻¹	555.8, 490.3, 366.8 and 286.8 mAh g ⁻¹ at 0.11, 0.21, 0.53, and 1.1 A g ⁻¹
SeS ₂ ²⁵	44	LGPS	Li	50 cycles, 89.2%, 0.05 A g ⁻¹	1450, 1329.5, 1282.7, and 1144.3 mAh g ⁻¹ at 0.44, 0.89, 1.33, and 2.23 A g ⁻¹	1024, 970, 949, and 887 mAh g ⁻¹ at 0.2, 0.4, 0.6, and 1 A g ⁻¹
S/PAN ²⁶	44	LCE	Li	50 cycles, 33.2%, 0.16 A g ⁻¹	1183, 719, and 482 mAh g ⁻¹ at 0.32, 0.8, and 1.6 A g ⁻¹	520.5, 316.4, 212.1 mAh g ⁻¹ at 0.14, 0.35, and 0.7 A g ⁻¹
S ²⁷	100	LPB	Li-In alloy	400 cycles, 89.9%, 0.16 A g ⁻¹	1144.6, 1024.0, 907.8, and 663.0 mAh g ⁻¹ at 0.16, 0.5, 0.83 and 1.675 A g ⁻¹	1144.6, 1024.0, 907.8, and 663.0 mAh g ⁻¹ at 0.16, 0.5, 0.83 and 1.675 A g ⁻¹
rGO@S ²⁸	40	LGPS	Li	93.5%, 30 cycles, 0.8 A g ⁻¹	1525.6, 1384.5, 1336.3, 903.2, 502.6, and 204.7 mAh g ⁻¹ at 0.08, 0.16, 0.83, 1.67, 3.34, and 8.37 A g ⁻¹	610.2, 553.8, 534.5, 361.3, 201, 81.9 at 0.03, 0.07, 0.33, 0.67, 1.34, 3.35 A g ⁻¹
Li ₂ S@Co-C@MHF ²⁹	65	SPE	Si@MHF	86%, 300 cycles, 0.23 A g ⁻¹	760, 650, 590, 520 mAh g ⁻¹ at 0.23, 0.58, 1.16, and 2.33 A g ⁻¹	494, 422, 383, 338 mAh g ⁻¹ at 0.15, 0.38, 0.75, and 1.51 A g ⁻¹
S _{9.3} I, Our work	70	LPS/L PSCI	Li	98.3% 50 th cycle, 96.9% 100 th cycle, 96.1% 200 th , 91.4% 300 th , 87% 400 th , 0.16 A g ⁻¹	1655.3, 1467.1, 1354.4, 1309, 1252.7, 1211.4, 1147.1, 1070, 978.3, 891.4, 699.1 at 0.23, 0.46, 0.68, 1.14, 1.83, 2.28, 3.43, 4.57, 5.71, 6.86 and 8.0 A g ⁻¹	1158.7, 1027, 948.1, 916.3, 876.9, 848, 803, 749, 684.8, 624, 489.4 at 0.16, 0.32, 0.48, 0.80, 1.28, 1.60, 2.40, 3.20, 4.00, 4.80 and 5.60 A g ⁻¹